JEM Journal of Experimental Medicine

ARTICLE

# Pro-inflammatory activation following demyelination is required for myelin clearance and oligodendrogenesis

Maria Inês Cunha[1,2,3*], Minhui Su[1,2*], Ludovico Cantuti-Castelvetri[1,2], Stephan A. Müller[2], Martina Schifferer[1,2], Minou Djannatian[1,2], Ioannis Alexopoulos[1,2], Franziska van der Meer[4], Anne Winkler[4], Tjakko J. van Ham[5], Bettina Schmid[2], Stefan F. Lichtenthaler[2,6,7], Christine Stadelmann[4], and Mikael Simons[1,2,6,8]

**Remyelination requires innate immune system function, but how exactly microglia and macrophages clear myelin debris after injury and tailor a specific regenerative response is unclear. Here, we asked whether pro-inflammatory microglial/macrophage activation is required for this process. We established a novel toxin-based spinal cord model of de- and remyelination in zebrafish and showed that pro-inflammatory NF-κB–dependent activation in phagocytes occurs rapidly after myelin injury. We found that the pro-inflammatory response depends on myeloid differentiation primary response 88 (MyD88). MyD88-deficient mice and zebrafish were not only impaired in the degradation of myelin debris, but also in initiating the generation of new oligodendrocytes for myelin repair. We identified reduced generation of TNF-α in lesions of MyD88-deficient animals, a pro-inflammatory molecule that was able to induce the generation of new premyelinating oligodendrocytes. Our study shows that pro-inflammatory phagocytic signaling is required for myelin debris degradation, for inflammation resolution, and for initiating the generation of new oligodendrocytes.**

## Introduction

Remyelination is a regenerative process that occurs naturally in demyelinated lesions proceeding through the processes of oligodendrocyte progenitor cell (OPC) proliferation and differentiation (Franklin and Ffrench-Constant, 2017). Remyelination can occur in diseases such as multiple sclerosis (MS) but often fails during the progressive phase of the disease (Dendrou et al., 2015; Reich et al., 2018). An unmet but urgent medical need is therefore the development of myelin repair–promoting therapies (Plemel et al., 2017). To achieve this goal, an understanding of the function of the cells of the innate immune system in myelin repair is critical. Damage to myelin triggers innate immune cell activation, including microglia and monocyte-derived macrophages, which respond by proliferating and migrating to the area of injury (Foote and Blakemore, 2005). The cellular response after injury occurs in distinct phases, starting with immune cell activation, followed by immune phenotype adaptation, and ending with resolution of the response (Miron et al., 2013; Dombrowski et al., 2017). While the innate immune system plays an important role in tissue repair, uncontrolled phagocyte activation can also cause tissue damage (Lloyd and Miron, 2019). A key open question is how the innate immune system instructs the regenerative process. In the case of myelin injury, the question arises whether and how phagocytes clearing away the damaged myelin initiate a specific response leading to OPC proliferation and differentiation. While the regenerative properties of microglia and macrophages have been recognized, it is unclear how the cells obtain information on the nature of the damaged target and how a tailored regenerative response is generated. A central theme in innate immune system biology is that sensing occurs by damage or pattern-recognition receptors such as the TLRs that recognize unique structures associated with infection or tissue damage (Takeda et al., 2003). For example, the difference in the outcome of phagocytosis of apoptotic cells and pathogens is due to the interaction of TLRs with

[1]Institute of Neuronal Cell Biology, Technical University Munich, Munich, Germany; [2]German Center for Neurodegenerative Diseases, Munich, Germany; [3]Graduate Program in Areas of Basic and Applied Biology, Abel Salazar Biomedical Sciences Institute, University of Porto, Porto, Portugal; [4]Department of Neuropathology, University of Göttingen Medical Center, Göttingen, Germany; [5]Department of Clinical Genetics, Erasmus MC, University Medical Center Rotterdam, Rotterdam, Netherlands; [6]Munich Cluster of Systems Neurology (SyNergy), Munich, Germany; [7]Neuroproteomics, School of Medicine, Klinikum rechts der Isar, Technical University of Munich, Munich, Germany; [8]Max Planck Institute of Experimental Medicine, Göttingen, Germany.

*M.I. Cunha and M. Su contributed equally to this paper; Correspondence to Mikael Simons: msimons@gwdg.de.

macromolecules of microbial origin, leading to activation of the transcription factors NF-κB and interleukin-1 receptor families, which dictate the outcome of the innate immune response (Hochreiter-Hufford and Ravichandran, 2013).

Here, we asked whether pro-inflammatory signaling is necessary to initiate the regenerative response that occurs upon demyelinating injury. TLRs constitute an extended family of proteins; thus, we decided to delete myeloid differentiation primary response 88 (MyD88), a universal adapter protein required for the induction of inflammatory cytokines downstream of all TLRs (except TLR3; Kawai and Akira, 2007). Given that many of the mechanisms that link inflammation to regeneration are evolutionary conserved (Tsarouchas et al., 2018), we employed a trans-species approach by combining work in zebrafish and mice in order to ask whether and how myelin phagocytosis induces the instructive inflammatory cell activation necessary for the regenerative response.

## Results

### Establishment of a lysolecithin (LPC)-induced model of spinal cord demyelination in zebrafish larvae

Focal demyelinating lesions can be induced in the white matter of mice and rats by local injection of LPC, a membrane-dissolving chemical (Jeffery and Blakemore, 1995; Kotter et al., 2006). Since zebrafish represent a highly versatile model system to study myelin biology, we wondered whether we could adapt the LPC-induced model of myelin injury to the spinal cord of zebrafish larvae. Using a stereotactic injection device, we injected a solution of 4 nl of LPC into the thoracic spinal cord of 6 d postfertilization (dpf) double transgenic Tg(*mbp:mCherry-CAAX*) and Tg(*mpeg1:eGFP*) larvae to visualize myelin sheaths and phagocytes, respectively. We used larvae at 6 dpf, as this represents an age when myelination in the spinal cord is largely completed and the population of resident phagocytes of the central nervous system (CNS) is already established. We observed a rapid recruitment of eGFP$^+$ phagocytes into the lesion site, with a peak of phagocyte infiltration at 2 d postinjection (dpi) and a progressive decline in the following 5 d (Fig. 1, A–C). PBS injection resulted in influx of phagocytes shortly after the injection, but numbers had already returned to baseline values at 2 dpi. We assessed myelination integrity by determining mCherry-CAAX signal in LPC-injected zebrafish larvae (see Materials and methods) and observed a reduction at 6 h postinjection (hpi) and 2 dpi, followed by an increase at 4 and 7 dpi. The drop in the signal at 2 dpi was not a result of bleaching, as it was only observed in LPC-injected and not in PBS-injected or noninjected fish (Fig. 1, A–C). In addition, the reduction in mCherry-CAAX signal was accompanied by a loss of myelinating oligodendrocytes as assessed by counting the number of eGFP$^+$ cells in Tg(*mbp:nls-eGFP*) that express eGFP in the nucleus of mature oligodendrocytes (Fig. 1, D and E). Furthermore, using Tg(*olig1:nls-mApple*) to assess the recruitment of OPCs, we found a decrease at 6 hpi and 1 dpi, which was followed by an increase back to normal numbers within the following days (Fig. 1, F and G).

To characterize the extent of axonal damage after LPC injections, we performed confocal imaging using Tg(*cntn1b:mCherry*) together with Tg(*mbp:eGFP-CAAX*) to visualize axonal and myelin loss in the same lesions. We found that LPC injections resulted in a reduction of mCherry-CAAX fluorescence signal by only ∼3%, while eGFP-CAAX signal dropped by ∼25% at 2 dpi. By serial scanning electron microscopy, we confirmed that only a small fraction of axons was lost in the lesions (∼4%, $n = 2$). Furthermore, using scanning electron microscopy at 2 dpi, we observed myelin fragments and phagocytes engulfing myelinated axons, providing further evidence that LPC injection results in demyelinating lesions. At 4 dpi, we observed demyelinated axons, but also axons with loose myelin wraps, possibly representing remyelination (Fig. 2, A–D).

Phagocytes play an important role in myelin debris clearance and in initiating the regenerative response in mice (Kotter et al., 2006; Miron et al., 2013; Cantuti-Castelvetri et al., 2018). To further validate the LPC-induced model of de- and remyelination in zebrafish, we used loss of function mutants in the colony-stimulating factor 1 receptor a and b (csf1ra and csf1rb), which are almost devoid of microglia (Oosterhof et al., 2018). When LPC-induced lesions were induced in *csf1ra*$^{-/-}$;*b*$^{-/-}$ (*csf1r*$^{-/-}$) mutant larvae and compared with WT controls, we observed that remyelination was impaired, providing evidence for a role of microglia in remyelination in the larval zebrafish spinal cord (Fig. 1, H and I). Thus, we have established an LPC-induced model of spinal cord demyelination in the larval zebrafish, characterized by rapid demyelination, phagocyte influx, and loss of oligodendrocytes, which is followed by repopulation of the lesion with oligodendrocytes and subsequent remyelination. The reproducible pattern of de- and remyelination, together with the conserved role of microglia/macrophages in myelin repair, allowed us to use this system to analyze the function of phagocytes in myelin repair.

### Impaired phagocyte resolution in spinal cord lesions of *myd88* mutant zebrafish

To determine whether pro-inflammatory signaling pathways are induced in phagocytes after myelin injury, we used double transgenic Tg(*NF-κb:eGFP*) and Tg(*mpeg1:mCherry-CAAX*) zebrafish. The Tg(*NF-κb:eGFP*) fish line was previously shown to serve as a sensitive reporter to monitor NF-κB activity (Kanther et al., 2011). Upon lesion induction, we found that there was a strong increase in eGFP signal in mCherry$^+$ phagocytes within 6 hpi, indicative of NF-κB activation. This was followed by a progressive decrease during the course of lesion evolution, providing evidence that NF-κB activation in phagocytes is an early event after myelin injury (Fig. 3, A and B). Myeloid differentiation factor 88 (Myd88) is a key adaptor for inflammatory signaling pathways downstream of TLRs, culminating in the activation of NF-κB signaling, resulting in the expression of cytokines, chemokines, and type I IFNs (Wesche et al., 1997). We used a *myd88* mutant zebrafish line (*myd88*$^{-/-}$; van der Vaart et al., 2013) to determine whether this key inflammatory signaling pathway is required for phagocyte activation in demyelinating lesions. When we injected LPC into the spinal cord of double transgenic Tg(*NF-κb:eGFP*) and Tg(*mpeg1:mCherry-CAAX*) *myd88*$^{-/-}$ zebrafish larvae, we found a pronounced reduction in eGFP within mCherry$^+$ phagocytes at 6 hpi and 2 dpi compared

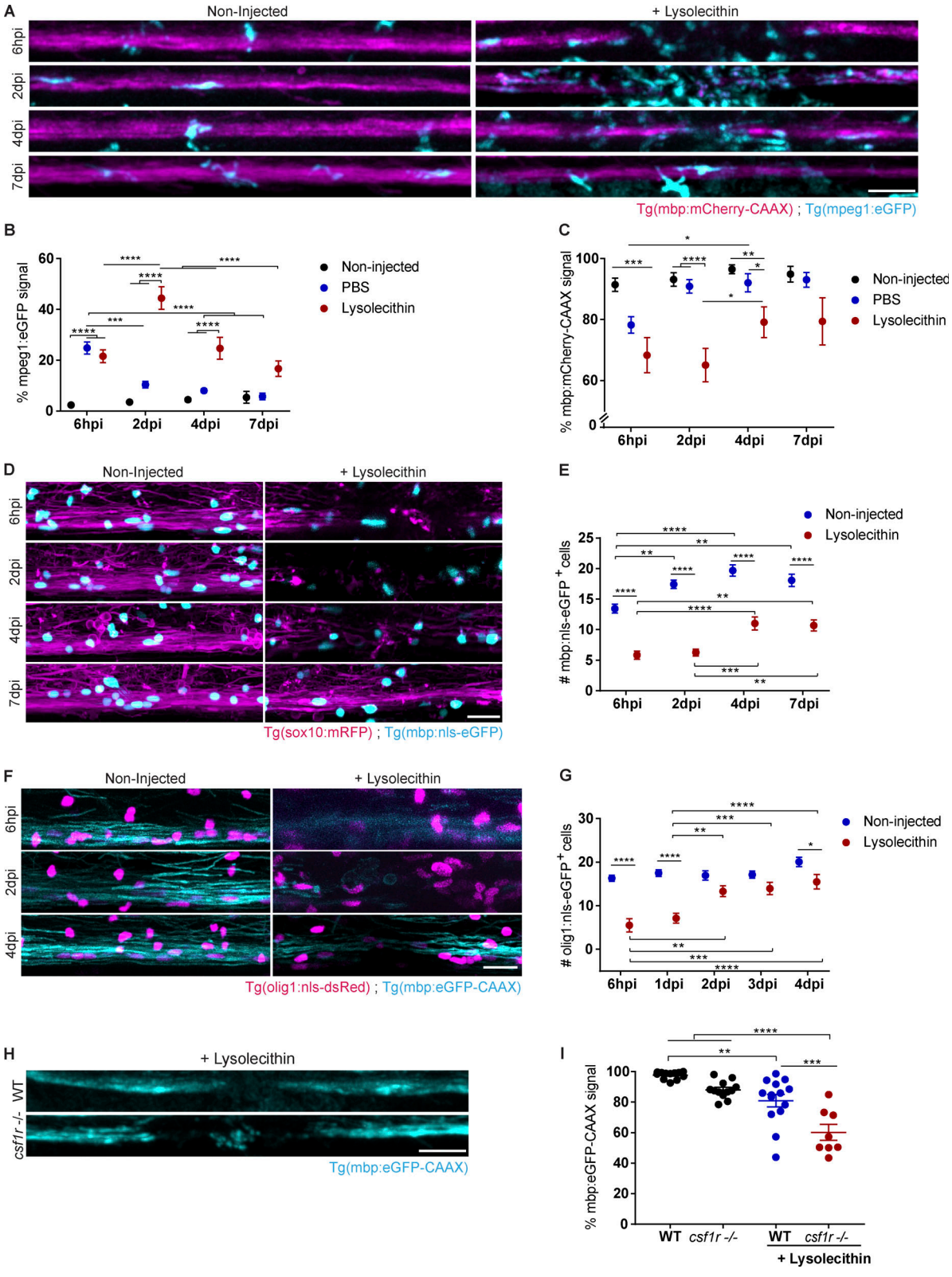


Figure 1. **The zebrafish larvae LPC model of de- and remyelination. (A–C)** Confocal maximum intensity z-projections of a spinal cord lesion show the myelinated spinal cord (magenta) and phagocytes (cyan) over time. Phagocyte infiltration was determined by the total amount of mpeg1:eGFP signal in the lesion. Myelination was determined by the total amount of mbp:mCherry-CAAX signal in the dorsal spinal cord. *n* = 9–12, 15–16, 13–20, and 4–8 animals at 6 hpi, 2 dpi, 4 dpi, and 7 dpi, respectively. **(D and E)** Confocal maximum intensity z-projections of a spinal cord lesion show the myelinated spinal cord (magenta) and the nuclei of mature oligodendrocytes (cyan) over time in noninjected larvae and larvae injected with LPC. The number of mature oligodendrocytes was determined by counting the mbp:nls-eGFP positive nuclei. *n* = 20–21, 16–21, 20–22, and 12–15 animals at 6 hpi, 2 dpi, 4 dpi, and 7 dpi, respectively. **(F and G)** Confocal maximum intensity z-projections of the spinal cord lesion show the myelinated spinal cord (cyan) and the nuclei of

oligodendrocyte precursor cells (magenta) over time in noninjected larvae and larvae injected with LPC. The number of OPCs was determined by counting the olig1:nls-mApple–positive nuclei. *n* = 8–10, 12–16, 16, 17, and 16 or 17 animals at 6 hpi, 1 dpi, 2 dpi, 3 dpi, and 4 dpi, respectively. **(H and I)** Confocal maximum intensity z-projections of the spinal cord lesion at 4 dpi show the myelinated spinal cord (cyan). Myelination was determined by the total amount of mbp:eGFP-CAAX signal in the dorsal spinal cord. *n* = 8–14 animals. Lateral views of the lesion site are shown; anterior is left and dorsal is down. All data are mean ± SEM (error bars). *, P < 0.05; **, P < 0.01; ***, P < 0.001; ****, P < 0.0001 by two-way ANOVA test in B, C, E, and G or one-way ANOVA in I, with Tukey's multiple comparisons test. Scale bars: 50 µm in A and H; 20 µm in D and F.

with control, showing that phagocyte activation is effectively suppressed (Fig. 3, A and B).

Next, we determined the recruitment of phagocytes into lesions of *myd88*$^{-/-}$ and control fish and found that it did not differ at 6 hpi and 2 dpi. However, when lesions were analyzed at 4 dpi, we observed a higher number of phagocytes in *myd88*$^{-/-}$ larvae than in control, suggesting that inflammation resolution is impaired in mutants (Fig. 5, A and B). To determine the underlying reason, we analyzed myelin debris clearance by phagocytes. Time-lapse imaging of double transgenic Tg(*mbp:mCherry-CAAX*) and Tg(*mpeg1:eGFP*) zebrafish showed that phagocytes were actively taking up and stripping off myelin from axonal tracts in LPC-induced lesions at 2 dpi in control fish (Fig. 3 C and Video 1). Hence, we assessed the accumulation of myelin debris, as determined by the incorporation of mCherry$^{+}$ myelin particles within eGFP$^{+}$ phagocytes and found that it was within a similar range in double transgenic Tg(*mbp:mCherry-CAAX*) and Tg(*mpeg1:eGFP*) *myd88*$^{-/-}$ and control fish at this time point, suggesting that phagocytosis was not visibly disturbed.

We then sought to determine the rate of myelin debris clearance by quantifying the amount of mCherry$^{+}$ myelin within eGFP$^{+}$ phagocytes in lesions at 2 and 4 dpi and found that control fish efficiently cleared away myelin debris. However, when this analysis was performed in *myd88*$^{-/-}$, accumulation of myelin debris was found within phagocytes at 4 dpi (Fig. 3, D and E). Because lysosomes are the organelles responsible for degradation, we analyzed whether lysosomal biogenesis was impaired in *myd88*$^{-/-}$ phagocytes. However, we found that the number of lysosomes in phagocytes that had declined in control lesions from 2 to 4 dpi, as determined by LysoTracker, remained high in *myd88*$^{-/-}$ fish at 4 dpi (Fig. 3, F and G). In noninjected larvae, eGFP$^{+}$ phagocytes were almost completely devoid of LysoTracker$^{+}$ lysosomes (Fig. S1, A and B).

To visualize how phagocytes were handling ingested myelin debris, we used time-lapse imaging to follow the phagocytes in 3 dpi lesions of *myd88*$^{-/-}$ and control fish. Although most cells were highly motile both in mutants and in controls, there were higher numbers of amoeboid and stationary phagocytes in *myd88*$^{-/-}$ fish (Fig. 3, H and I; and Videos 2 and 3). Collectively, these data provide evidence that phagocytes in *myd88*$^{-/-}$ zebrafish larvae are able to phagocytose myelin but fail to degrade myelin debris after the uptake has occurred.

### Myelin clearance is impaired in MyD88-deficient microglia

To understand the roles of pro-inflammatory signaling in a mammalian model of demyelination, we performed LPC injections into the spinal cord of WT and MyD88-deficient mice. In lesioned animals, demyelination is normally complete within 4 d, followed by a repair process that occurs in WT animals between 7 and 21 dpi (Keough et al., 2015; Wang and Kotter, 2018). Using Luxol Fast Blue staining, we found that lesion sizes at 4 dpi were similar in WT and *Myd88*$^{-/-}$ mice (Fig. S1, C and D). Next, we used immunohistochemistry (IHC) to determine the number of IBA1$^{+}$ phagocytes. We found that the density of IBA1$^{+}$ cells did not differ at 4 and 7 dpi in lesions of WT and MyD88-deficient mice (Fig. S1, E–H). However, when lesions were analyzed at 14 dpi, we observed a higher density of IBA1$^{+}$ phagocytes in lesions of MyD88-deficient mice (Fig. 4, A and B). In addition, there was an increase in the total number of IBA1$^{+}$ phagocytes with accumulation of intracellular FluoroMyelin$^{+}$ myelin debris within mutant lesions (Fig. 4 C), although the percentage of FluoroMyelin$^{+}$/IBA1$^{+}$ phagocytes was not statistically significantly altered between WT and mutant mice (Fig. 4 D).

To determine the mechanism of impaired myelin clearance, we prepared primary cultures of microglia from WT and MyD88-deficient mice and performed myelin debris phagocytosis assays. To ensure that most myelin debris were internalized by the cells, microglia cultures were treated with myelin for 2 h, and the degradation was assayed in the following 6 and 24 h. While the amount of internalized myelin debris did not differ directly after the uptake, we found a slower decrease of FluoroMyelin$^{+}$ myelin debris in MyD88-deficient microglia at 6 and 24 h after internalization (Fig. 4, E and F). After phagocytosis has occurred, phagosomes rapidly fuse with lysosomes, forming phagolysosomes, which can be labeled by LysoTracker. Thus, the extent of phagosome-to-lysosome fusion can be assayed by determining the colocalization of the internalized cargo with lysosomes shortly after the uptake. We used PKH67 to label myelin debris and LysoTracker to mark lysosomes and observed fewer myelin-PKH67$^{+}$LysoTracker$^{+}$ phagosomes in MyD88-deficient microglia (Fig. 4, G–I). A crucial reaction during and after the uptake of phagocytic cargo is the activation of the respiratory burst pathway, which leads to the release of ROS required to break down the phagocytic material and to promote phagosome maturation. We determined the extent of respiratory burst induction after myelin debris uptake in WT and MyD88-deficient microglia by quantifying ROS. We found a significant reduction in ROS-derived signal colocalizing with myelin debris particles in MyD88-deficient microglia compared with WT microglia, as determined by the OxyBURST assay (Fig. 4, J–L). In summary, these data provide evidence for impaired myelin debris degradation within the phagolysosomal pathway of MyD88-deficient microglia.

### Oligodendrogenesis and remyelination are impaired after LPC-induced myelin injury in MyD88 mutant zebrafish and mice

To determine the impact of impaired phagocyte resolution on remyelination, we injected LPC into the spinal cord of double

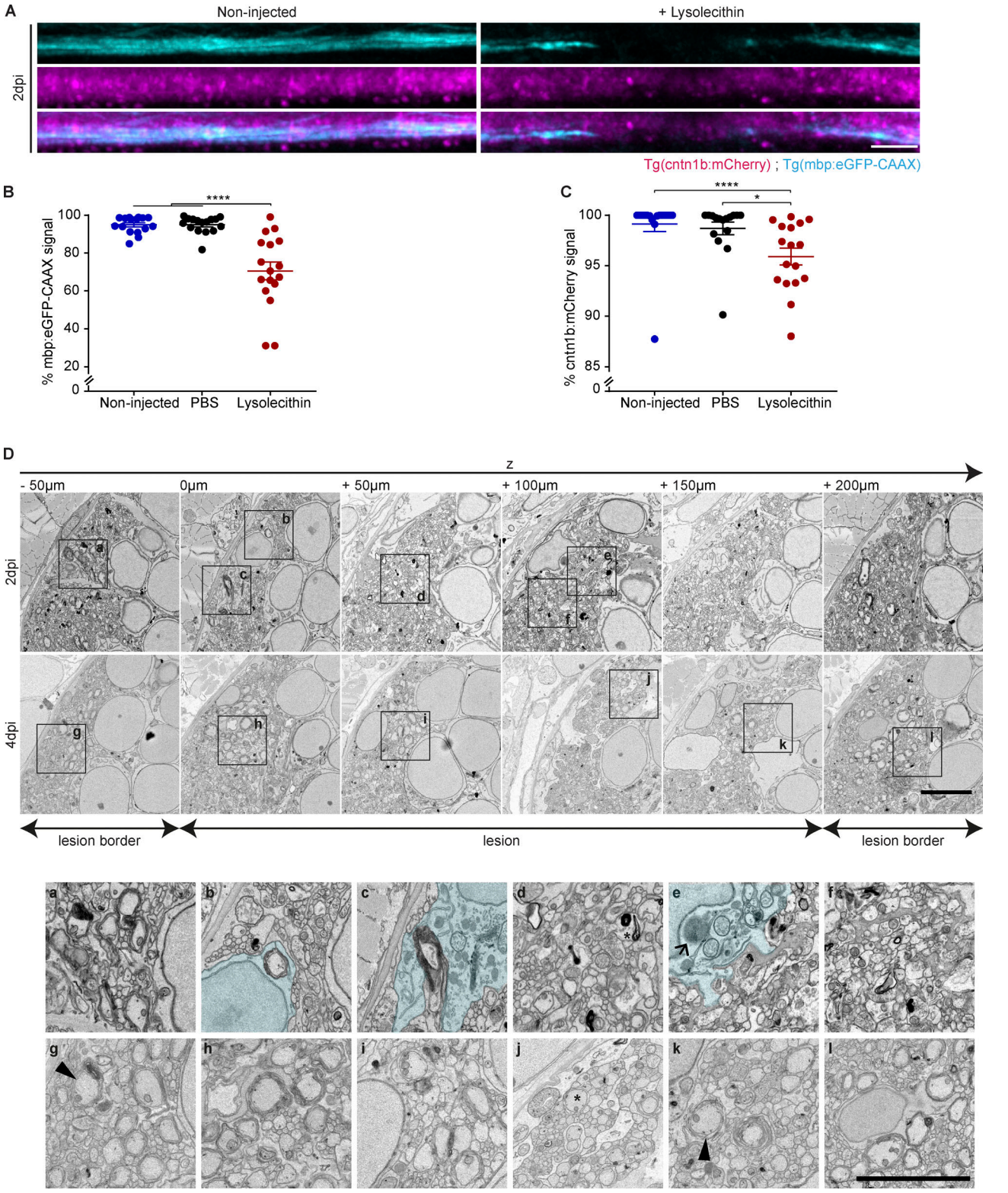


Figure 2. **Characterization of myelin and axonal damage in the zebrafish larvae LPC model. (A–C)** Confocal maximum intensity z-projections of the spinal cord show the myelinated spinal cord (cyan) and the axons (magenta) at 2 dpi in noninjected larvae and larvae injected with LPC. *n* = 16 or 17 animals. **(D)** Electron micrographs of serial cross sections of the spinal cord lesion at 2 and 4 dpi in WT larvae injected with LPC. **(D, a, b, and d–f)** Close-up images showing myelin fragments in a demyelinating lesion at 2 dpi. **(D, b and c)** Close-up images showing a phagocyte (blue) engulfing myelinated axons at 2 dpi. **(D, c and e)** Close-up images showing lysosomes inside phagocytes (arrow in e) at 2 dpi. **(D, b, d, f, and j)** Close-up images showing demyelinated axons (asterisks in d and j, at 2 and 4 dpi, respectively). **(D, g, h, j, and k)** Close-up images showing the presence of partially myelinated axons at 4 dpi (arrowheads in g and k). All data are mean ± SEM (error bars). *, P < 0.05; ****, P < 0.0001 by one-way ANOVA, with Tukey's multiple comparisons test in B or Kruskal-Wallis test with Dunn's multiple comparisons test in C. Scale bars: 50 µm in A; 5 µm in D.

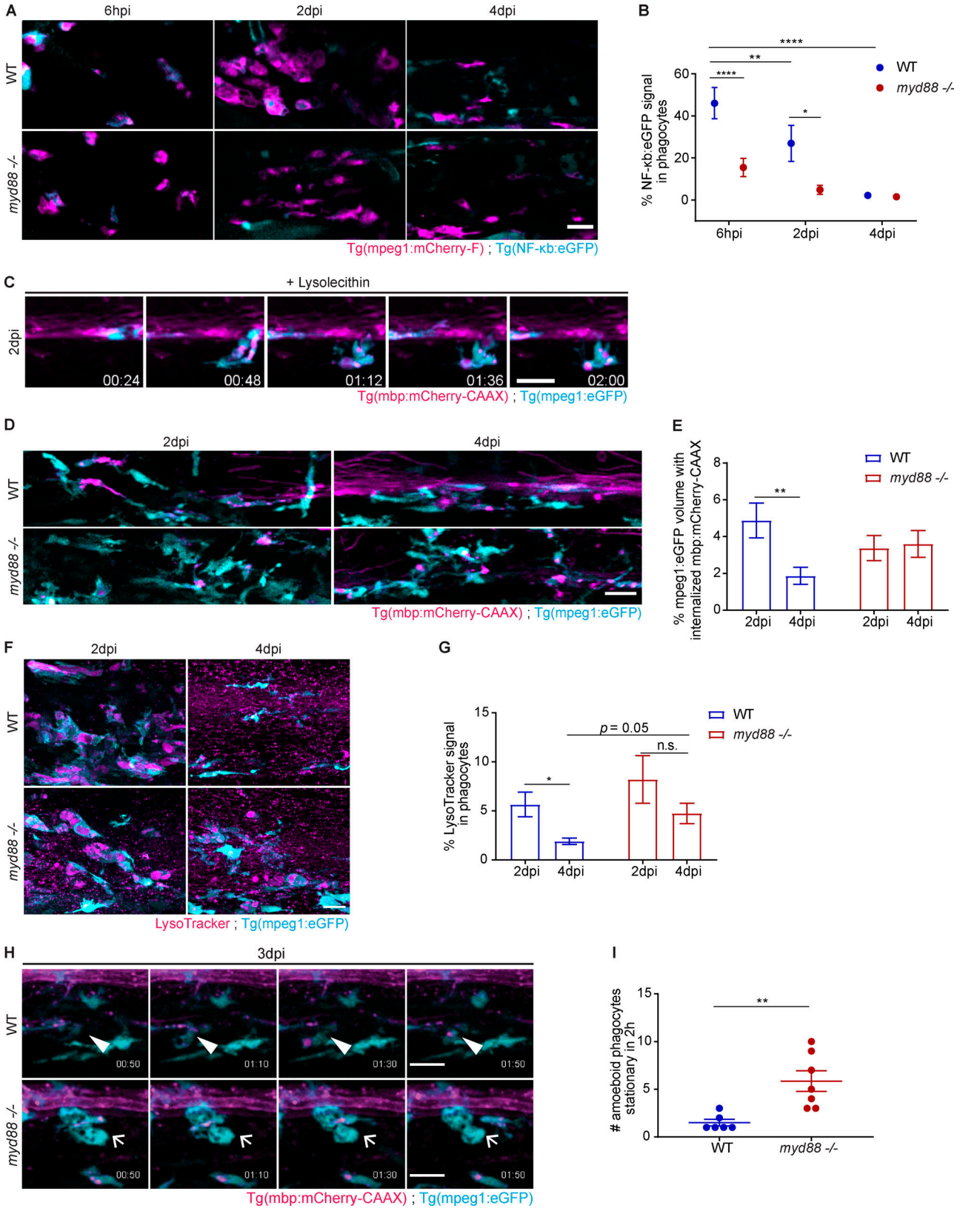


Figure 3. **Delayed clearance of ingested myelin debris by *myd88*$^{-/-}$ phagocytes in zebrafish larvae. (A and B)** Confocal z-sections of a spinal cord lesion show NF-κB activation (cyan) in recruited phagocytes (magenta) over time. NF-κB activation was determined by the colocalized signal of NF-κb:eGFP with mpeg1:mCherry. *n* = 9 or 10, 7, and 10 or 11 animals at 6 hpi, 2 dpi, and 4 dpi, respectively. **(C)** Confocal maximum intensity z-projections from a 2 h time-lapse video (Video 1) of the spinal cord lesion at 2 dpi showing the myelinated spinal cord and myelin debris (magenta) and phagocyte (cyan) movement in WT larvae. **(D and E)** Confocal maximum intensity z-projections of the spinal cord lesion at 2 dpi and 4 dpi show the myelinated spinal cord and myelin debris (magenta) in

phagocytes (cyan). The amount of internalized myelin was determined by the colocalized signal of mbp:mCherry-CAAX within mpeg1:eGFP. *n* = 11–15 and 15–17 animals at 2 and 4 dpi, respectively. **(F and G)** Confocal maximum intensity z-projections of the spinal cord lesion at 4 dpi, showing lysosomes (magenta) in phagocytes (cyan). The amount of lysosomes was determined by the colocalized signal of LysoTracker with mpeg1:eGFP. *n* = 8–10 and 14–25 animals at 2 and 4 dpi, respectively. **(H and I)** Confocal maximum intensity z-projections from 2 h time-lapse videos (Videos 2 and 3) of the spinal cord lesion at 3 dpi show the myelinated spinal cord and myelin debris (magenta) and phagocyte (cyan) movement. Arrowheads show actively moving phagocytes, and short arrows show amoeboid stationary phagocytes. *n* = 6 or 7 animals. Lateral views of the lesion site are shown; anterior is left and dorsal is down. All data are mean ± SEM (error bars). *, P < 0.05; **, P < 0.01; ****, P < 0.0001; n.s. indicates no significance, by two-way ANOVA test with Tukey's multiple comparisons test in B, D, and E or Sidak's multiple comparisons test in G and unpaired *t* test with Welch's correction in J. Scale bars: 20 µm.

transgenic Tg(*mpeg1:eGFP*) and Tg(*mbp:mCherry-CAAX*) *myd88* mutant and control larval zebrafish and determined the myelinated area over time. We found that the reduction in myelinated area associated with demyelination at 6 hpi and 2 dpi was not different in *myd88* mutant and control fish. Demyelination is followed by remyelination, which can be visualized by the subsequent recovery of mCherry-CAAX signal. While signal increase was observed in control fish at 4 dpi, it did not recover in *myd88* mutant fish (Fig. 5, A and C). We further analyzed myelinating oligodendrocytes at 4 dpi using double transgenic Tg(*sox10:mRFP*) and Tg(*mbp:nls-eGFP*) fish that express eGFP in the nucleus of oligodendrocytes and found that the number of mature oligodendrocytes also did not recover in *myd88* mutants compared with control (Fig. 5, D and E). To determine whether this was a consequence of lack of early progenitor cells, we induced lesions in double transgenic Tg(*mbp:eGFP-CAAX*) and Tg(*olig1:nls-mApple*) larvae and found that mutants showed reduced nls-mApple$^+$ OPCs within lesions (Fig. 5, F and G). Non-injected *myd88* mutants did not show any signs of defective myelination (Fig. S2, A–I).

In mice, LPC-induced lesions become repopulated with OPCs that differentiate into myelinating oligodendrocytes starting at ∼7 dpi. We used antibodies against NKX-2.2 to assess the number of OPCs, against BCAS1 to visualize premyelinating and myelinating oligodendrocytes (Fard et al., 2017) and against APC (CC1) to mark mature oligodendrocytes in 7 and 21 dpi lesions. Lesions in WT mice were populated by NKX-2.2$^+$ OPCs and BCAS1$^+$ (pre)myelinating oligodendrocytes at 7 dpi. At 21 dpi, there was a decline in the number of OPCs and (pre)myelinating oligodendrocytes, which was accompanied by an increase in mature CC1$^+$ oligodendrocytes. In contrast, a strikingly different pattern was observed in the lesions of MyD88-deficient mice. There were significantly fewer NKX-2.2$^+$ OPCs and BCAS1$^+$ premyelinating and myelinating oligodendrocytes at 7 dpi and reduced formation of mature CC1$^+$ oligodendrocytes at 21 dpi (Fig. 6, A–F).

To assess the extent of remyelination, we performed methylene blue-azure II stain on semi-thin sections and found that remyelination, as determined by the formation of thin myelin sheaths on axons within the lesioned area, was severely impaired in MyD88-deficient mice (Fig. 6, G and H). However, no impairment of oligodendrogenesis was observed in MyD88-deficient mice during postnatal development (Fig. S3, A–D). In addition, the extent and morphology of myelin were indistinguishable between WT and Myd88-deficient adult mice (Fig. S3, E and F). Myelin thickness, as determined by g-ratio analysis, did also not reveal any differences (Fig. S3 G), suggesting that MyD88 signaling is specifically required for myelin regeneration. Collectively, these data from zebrafish and mice provide evidence that remyelination, but not myelination, is impaired in MyD88 mutants.

### TNF-α promotes oligodendrogenesis

MyD88-dependent inflammatory signaling pathways trigger the generation of cytokines, chemokines, and growth factors. To examine whether myelin debris phagocytosis in microglia induces the secretion of proteins that regulate oligodendrogenesis, we performed proteome analyses. WT and MyD88-deficient microglia cultured under serum-free media supplemented with 0.2% BSA were incubated with purified myelin debris for 4 h to induce phagocytosis, followed by a 16-h chase before harvesting the samples for mass spectrometry analysis. We compared differences in protein abundance in WT and MyD88-deficient microglia treated with myelin debris or not. Using $\log_2$ fold change of ±0.5 (>1.41-fold or <0.71-fold) and a P value <0.05 as a cutoff with false discovery rate (FDR) correction, we did not detect any differentially expressed proteins in untreated WT and MyD88-deficient microglia (Fig. 7 A). However, the treatment with myelin debris induced a distinct response in WT and MyD88-deficient microglia (Fig. 7, B and C). Treatment of WT microglia with myelin resulted in the up-regulation of 85 proteins, among which 49 were also significantly induced by myelin in MyD88-deficient microglia (Table S1 and Table S3; and Fig. S4, A and B). Many of these proteins, both in WT and MyD88-deficient microglia, are associated with lipid metabolism, such as PLIN2, ABCG1, APOE, ABCA1, and SOAT1 (Table S1 and Table S2). However, Ingenuity Pathway Analysis identified 10 significant pathways that were oppositely regulated in MyD88-deficient microglia compared with WT cells after myelin treatment. TNF-α, type II interferon, and peroxisome proliferated-activated receptor signaling were among the major pathways that failed to be activated in MyD88-deficient microglia (Fig. 7 D).

TNF-α is a pro-inflammatory cytokine released by immune cells and astrocytes in inflammatory CNS lesions, and concentrations are elevated in active lesions of patients with MS (Han et al., 2008). Addition of TNF-α to cultured oligodendrocytes and overexpression of TNF-α in astrocyte-transgenic mice have been shown to induce oligodendrocyte cell death and myelin vacuolization (Akassoglou et al., 1998). However, there is also evidence that TNF-α signaling promotes oligodendrocyte formation and remyelination (Arnett et al., 2001). To examine the expression of TNF-α in LPC-induced demyelinating lesions, we performed in situ hybridization in mouse spinal cord lesions and observed that LPC-induced myelin injury induced TNF-α transcription to a greater extent in lesions of WT mice than in MyD88-deficient mice (Fig. 8, A and B). To identify the source of injury-induced TNF-α expression, we performed RNAscope against TNF-α combined

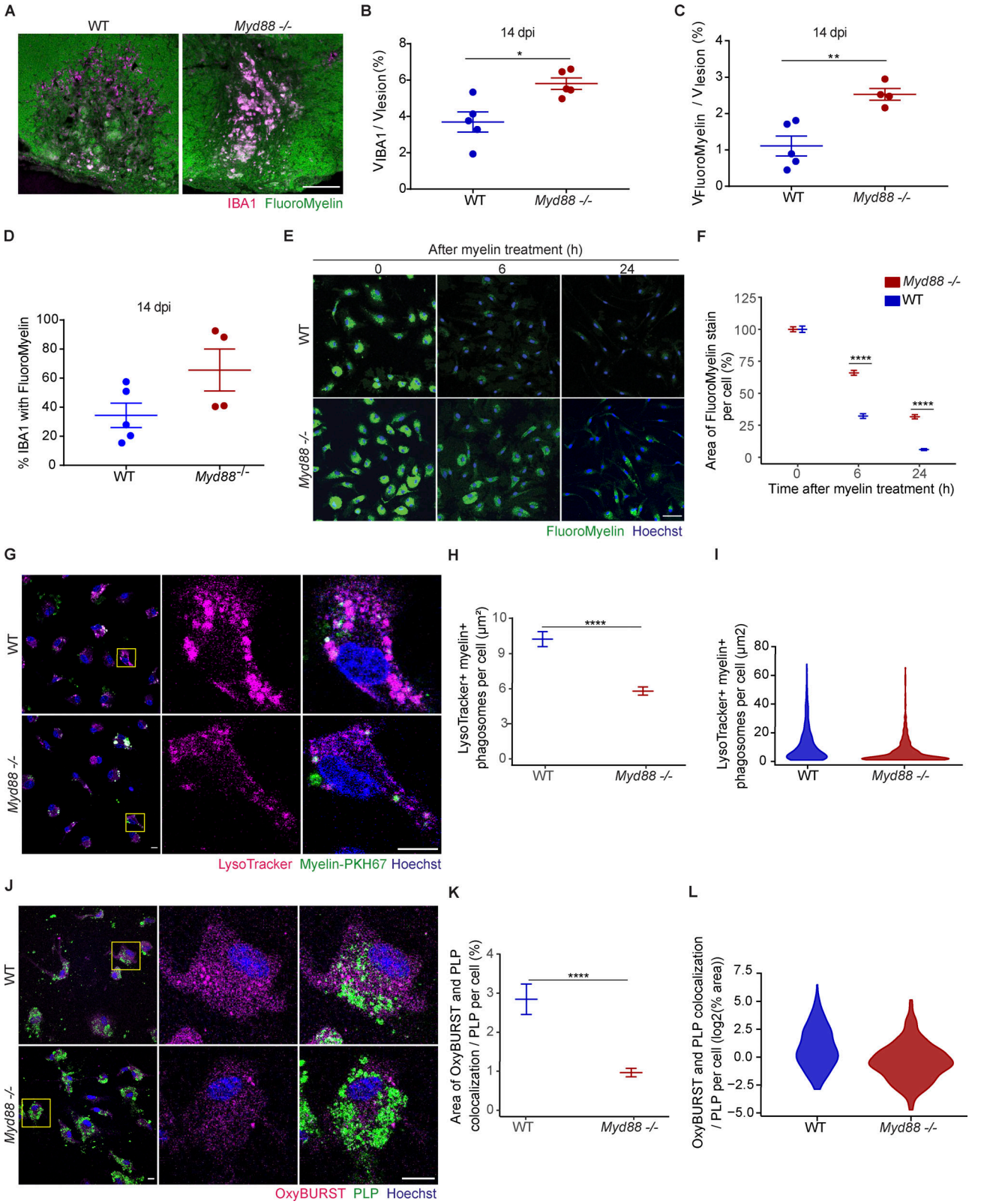


Figure 4. **Phagocyte retention in LPC-induced lesions of *Myd88*$^{-/-}$ mice and impaired phagosome maturation. (A and B)** Proportion of the volume occupied by IBA1$^{+}$ cells in the lesions (devoid of FluoroMyelin) of WT and *Myd88*$^{-/-}$ mice at 14 dpi. *n* = 4 or 5 lesions. **(C and D)** Total accumulation of myelin lipids in IBA1$^{+}$ cells in mouse spinal cord lesions at 14 dpi, analyzed by the proportion of the volume (V) occupied by both FluoroMyelin (green) and IBA1 (magenta; colocalization, white), shown in A, in the lesions (C) and analyzed per total amount of IBA1 signal (D). *n* = 4 or 5 lesions. **(E and F)** Degradation of myelin lipids in cultured microglia. The area of FluoroMyelin in each cell was normalized to the average area of FluoroMyelin per cell at the initial time point (0 h after myelin treatment). *n* = 3 independent experiments. 6 h after myelin treatment *Myd88*$^{-/-}$ versus WT: $P < 2.2 \times 10^{-16}$; effect size (Cohen's *d*) = 0.542;

1,188 *Myd88*$^{-/-}$ cells and 1,016 WT cells. 24 h after myelin treatment: *Myd88*$^{-/-}$ versus WT: $P < 2.2 \times 10^{-16}$; effect size (Cohen's *d*) = 0.657; 988 *Myd88*$^{-/-}$ cells and 947 WT cells. **(G–I)** Phagosome maturation in myelin-loaded microglia. **(G)** Myelin$^{+}$ phagosomes (myelin labeled with PKH67, green) and endolysosomes (LysoTracker Red$^{+}$, magenta) were detected by live-cell imaging. **(H and I)** Fusion of phagosomes containing myelin debris with endolysosomes, as analyzed by the area of the overlap between myelin debris and LysoTracker in each cell, 1 h after treatment with myelin debris. *n* = 3 independent experiments. *Myd88*$^{-/-}$ versus WT: $P = 1.911 \times 10^{-9}$; effect size (Cohen's *d*) = −0.430; 573 *Myd88*$^{-/-}$ cells and 352 WT cells. **(J–L)** Oxidative activity in cultured microglia after phagocytosing myelin debris. Representative overview and inset. The organelles labeled with OxyBURST BSA (magenta) identified ROS. Internalized myelin debris was identified by PLP (green). *n* = 3 independent experiments. *Myd88*$^{-/-}$ versus WT: $P = 4.388 \times 10^{-6}$; effect size (Cohen's *d*) = −0.345; 750 *Myd88*$^{-/-}$ cells and 378 WT cells. Data are mean ± SEM (error bars) in B, C, and D and 95% CI in F, H, and K. *, P < 0.05; **, P < 0.01; ****, P < 0.0001 by unpaired *t* test with Welch's correction in B, C, F, H, and K. Scale bars: 100 µm in A; 50 µm in E; and 10 µm in G and J.

with immunohistochemistry against IBA1 at 4 dpi and found that ∼80% of the TNF-α–positive cells colocalized with IBA1 (Fig. S5). In addition, real-time PCR of zebrafish spinal cord lesions showed that TNF-α mRNA expression was induced in lesions of control but to a much lesser degree in *myd88* mutant zebrafish (Fig. 8 C). Thus, TNF-α represents a candidate cytokine induced in phagocytes after demyelinating injury that may regulate oligodendrogenesis.

To determine the effects of TNF-α on the formation of new oligodendrocytes, organotypic cerebellar slice cultures (OCSCs) were treated with recombinant TNF-α and 5-ethynyl-2′-deoxyuridine (EdU) and immunostained with antibodies against OLIG2 and BCAS1 to quantify the number of newly generated and premyelinating and myelinating oligodendrocytes, respectively. We observed a marked induction of EdU$^{+}$BCAS1$^{+}$ and of EdU$^{+}$OLIG2$^{+}$ oligodendrocytes (Fig. 8, D–G). Furthermore, we performed stereotactic injections of TNF-α into the cortex of WT mice and performed IHC 5 d after the injections. As observed in the slice culture experiments, we detected a striking increase in the number of premyelinating BCAS1$^{+}$ oligodendrocytes upon TNF-α injections (Fig. 8, H–J). We also assessed the effect of TNF-α in promoting myelin debris clearance in microglia. When microglia cultures were treated with myelin for 2 h and the degradation of PLP was assayed in the following 6 h, we found that TNF-α was able to enhance degradation (Fig. 8, K and L). Finally, we determined whether TNF-α is able to rescue lesion recovery in the absence of MyD88. We used OCSCs, which we treated for 16 h with LPC, as an established ex vivo model of demyelination (Birgbauer et al., 2004; Zhang et al., 2011). After LPC treatment, we exchanged the medium and continued the incubation with or without recombinant TNF-α for 48 h, followed by immunostaining against BCAS1 to determine the number of premyelinating and myelinating oligodendrocytes. We found that BCAS1 immunoreactivity increased in WT but not Myd88-deficient slices 48 h after LPC treatment (Fig. 8, M and N). However, when TNF-α was added into the medium, we observed an increase in BCAS1 immunoreactivity in Myd88-deficient slices. Notably, TNF-α treatment of WT slices did not result in a further increase in BCAS1 immunoreactivity (Fig. 8, M and N). Thus, our data provide evidence that MyD88-dependent signaling induces the expression of TNF-α after a demyelinating injury, which is able to promote myelin debris degradation and the formation of new oligodendrocytes.

## Discussion

In this study, we provide evidence that pro-inflammatory activation is required for myelin debris degradation and for oligodendrogenesis after myelin injury. We used mice and zebrafish lacking MyD88, the canonical adaptor for inflammatory signaling pathways downstream of TLRs, and found that lesioned animals are impaired not only in phagosome maturation and myelin debris clearance but also in initiating the regenerative response necessary for the generation of new oligodendrocytes. We identified TNF-α as one factor that is produced to a lesser extent in lesions from MyD88-deficient mice and zebrafish and is able to promote efficient OPC generation. Our study underscores the role of microglia/macrophage activation in clearing myelin debris and initiating the secretion of pro-regenerative molecules for myelin repair. Our study concurs with earlier work, in which a role for innate immune cells and mediators in stimulating remyelination was shown (Miron et al., 2013). It is now well known that phagocytes are important for the rapid clearance of myelin debris to remove repulsive signals and to pave the way for oligodendrocyte differentiation and remyelination (Kotter et al., 2006; Syed et al., 2011). Such regenerative properties have been associated with anti-inflammatory, immune-regulatory M2 microglia/macrophages, which secrete growth factors that drive OPC differentiation (Miron et al., 2013; Lloyd et al., 2019). Thus, it is conceivable that the initial pro-inflammatory response is required to activate OPC proliferation and survival, while polarization of phagocytes into an anti-inflammatory phenotype that occurs later during lesion evolution is important to generate the factors for OPC differentiation (Miron et al., 2013). Pro-inflammatory activation of microglia and macrophages has long been implicated in inducing harm to the CNS by secreting damage-inducing molecules such as pro-inflammatory cytokines or ROS (Block et al., 2007; Perry and Teeling, 2013). This Janus-faced nature of activated microglia is particularly striking in active MS lesions, in which areas of active de- and remyelination coexist. TNF-α is one example of a pro-inflammatory factor with such a dual role.

A major question will be to resolve how TNF-α regulates pro-survival and proliferative responses as opposed to programmed cell death pathways. Studies in experimental autoimmune encephalomyelitis have shown that the blockage of TNF-α leads to reduced pathology (Brambilla et al., 2011; Steeland et al., 2017). One possibility is that the aggravating effects of TNF-α are mediated by interaction with TNFR1, while the pro-regenerative effects are attributed to signaling through TNFR2. One study suggested that the transmembrane form of TNF-α was responsible for promoting remyelination by engagement of TNFR2, while soluble TNF-α inhibited myelin repair (Karamita et al., 2017). Our data show that injection of soluble TNF-α into the mouse cortex or addition onto myelinating slice cultures was

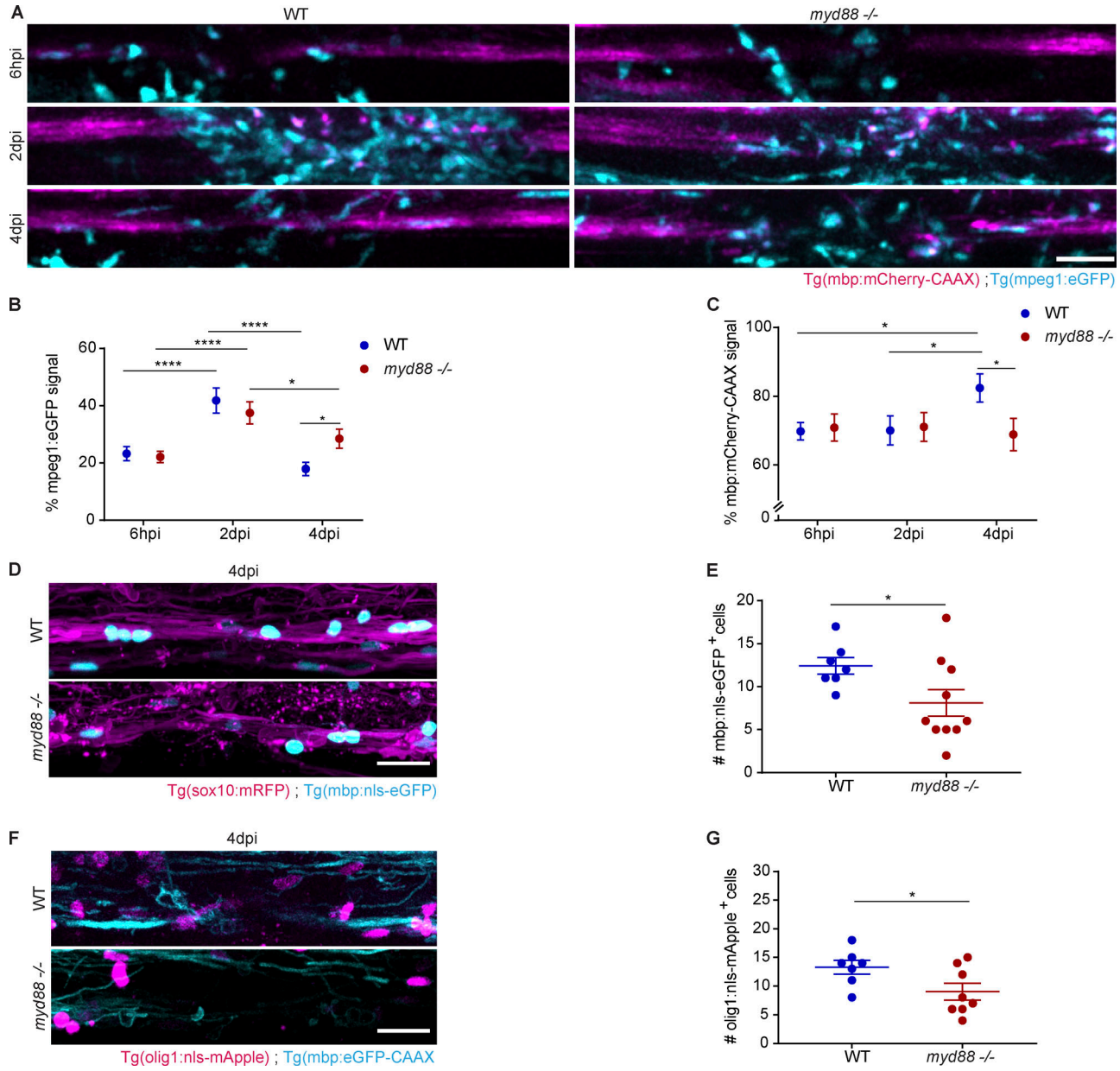


Figure 5. **Delayed phagocyte efflux in *myd88*$^{-/-}$ zebrafish larvae with impaired remyelination. (A–C)** Confocal maximum intensity z-projections of the spinal cord lesion over time show the myelinated spinal cord (magenta) and phagocytes (cyan) in WT and *myd88*$^{-/-}$ larvae injected with LPC. Phagocyte infiltration was determined by the total amount of mpeg1:eGFP signal in the lesion. Myelination was determined by the total amount of mbp:mCherry-CAAX signal in the dorsal spinal cord. *n* = 15–19, 11–17, and 13–17 animals at 6 hpi, 2 dpi, and 4 dpi, respectively. **(D and E)** Confocal maximum intensity z-projections of the spinal cord lesion at 4 dpi show the myelinated spinal cord (magenta) and the nuclei of mature oligodendrocytes (cyan). The number of mature oligodendrocytes was determined by counting the number of mbp:nls-eGFP–positive nuclei. *n* = 7 or 10 animals. **(F and G)** Confocal maximum intensity z-projections of the spinal cord lesion at 4 dpi show the myelinated spinal cord (cyan) and the nuclei of OPCs (magenta). The number of OPCs was determined by counting the number of olig1:nls-mApple–positive nuclei. *n* = 7 or 8 animals. Lateral views of the lesion site are shown; anterior is left and dorsal is down. All data are mean ± SEM (error bars). *, P < 0.05; ****, P < 0.0001 by two-way ANOVA test, with Tukey's multiple comparisons test in B and C and unpaired *t* test with Welch's correction in E and G. Control noninjected larvae WT and *myd88*$^{-/-}$ animals are included in the statistical analysis in B and C and are represented in Fig. S3, A–C. Scale bars: 50 µm in A; 20 µm in D and F.

sufficient to induce the generation of (pre)myelinating BCAS1$^{+}$ oligodendrocytes. This pro-regenerative effect of TNF-α may explain why clinical trials in MS using recombinant TNFR or antibodies against TNF-α were not only ineffective, but even worsened the disease in some patients (van Oosten et al., 1996).

Recently, single-nucleus RNA sequencing from postmortem human brain from patients with MS and from unaffected controls revealed a depletion of OPCs in MS (Jäkel et al., 2019). Furthermore, studies using $^{14}$C carbon dating in human tissue provided little evidence for OPC proliferation in fully remyelinated shadow plaques. In contrast, OPC proliferation was clearly

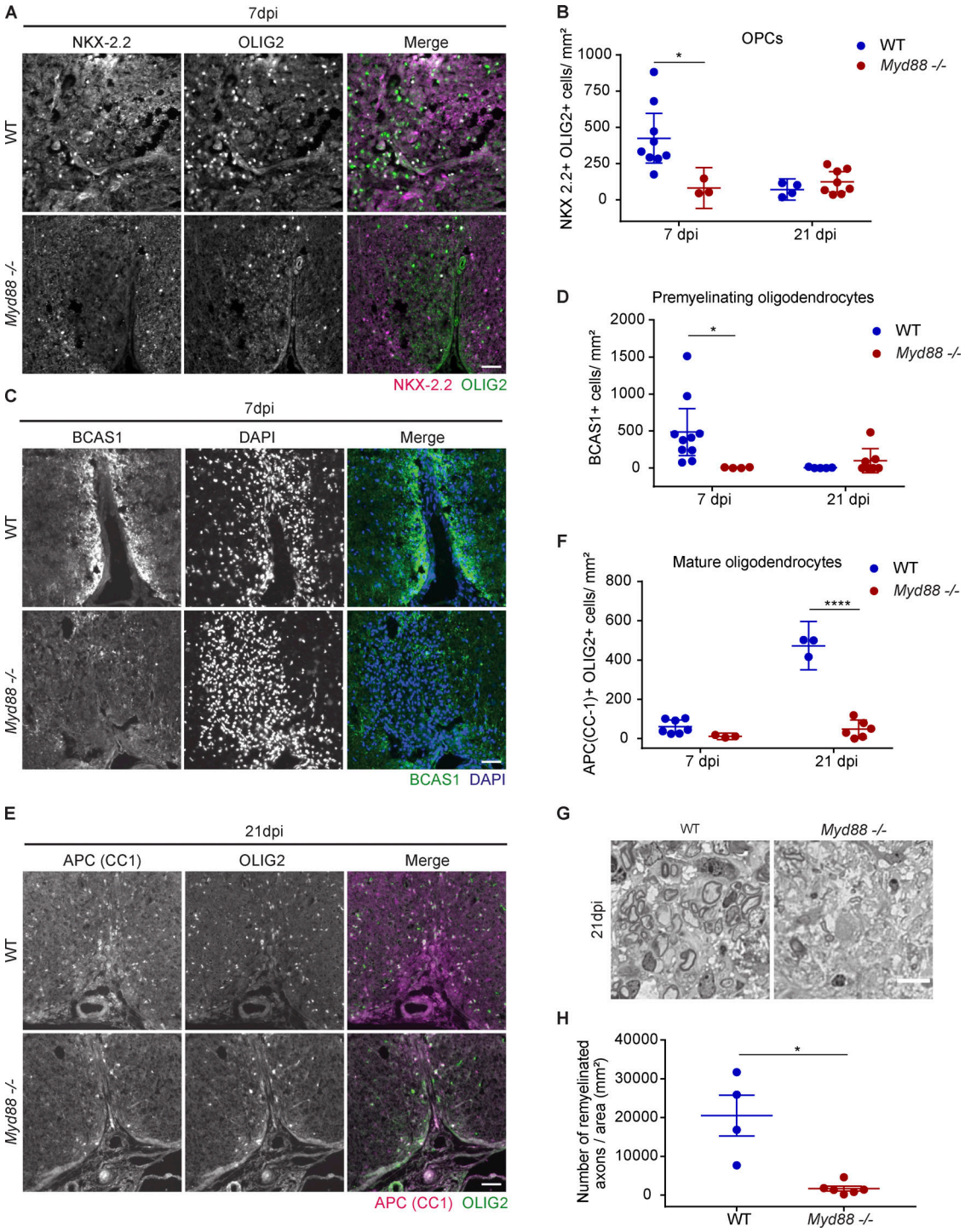


Figure 6. **Defective remyelination in the spinal cord of *Myd88*$^{-/-}$ mice. (A and B)** OPCs in demyelinated lesions in mouse spinal cords at 7 dpi. The nuclei of OPCs were identified by the expression of both NKX-2.2 (magenta) and OLIG2 (green; colocalization, white). *n* = 3–9 lesions. **(C and D)** Premyelinating oligodendrocytes expressing BCAS1 (green) in mouse spinal cord lesions at 7 dpi. *n* = 4–10 lesions. **(E and F)** Mature oligodendrocytes expressing both APC (CC1; magenta, cytoplasm) and OLIG2 (green, nucleus) in mouse spinal cord lesions at 21 dpi. *n* = 3–7 lesions. **(G and H)** Remyelination in mouse spinal cord lesions at 21 dpi, quantified by the density of remyelinated axons in semi-thin sections. *n* = 4–6 lesions. Data are mean ± 95% CI (error bars) in B, D, and F or SEM in H. *, P < 0.05; ****, P < 0.0001 by two-way ANOVA test, with Sidak's multiple comparisons test in B, D, and F and unpaired *t* test with Welch's correction in H. Scale bars: 100 µm in A, C, and E; 10 µm in G.

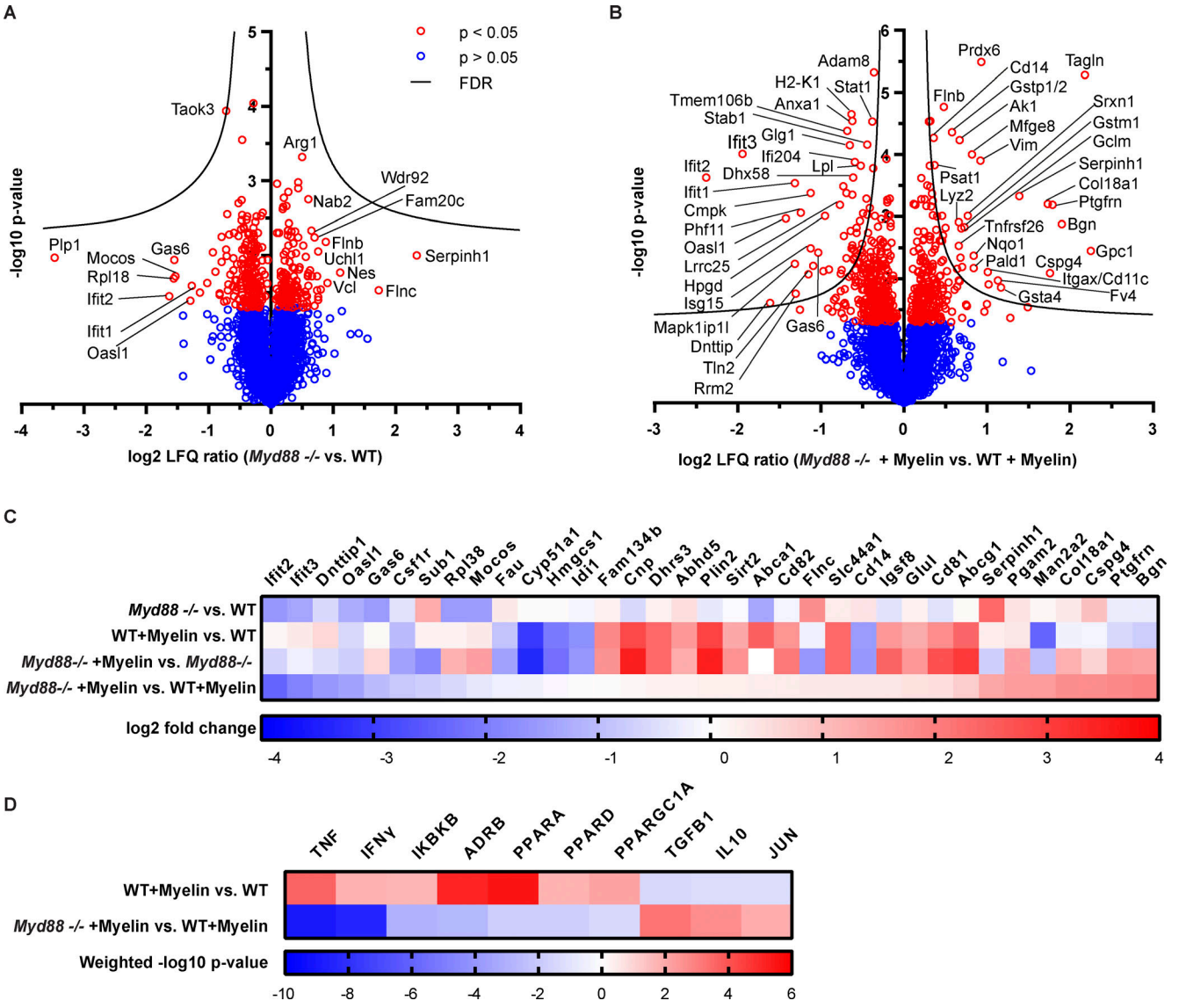


Figure 7. **Proteome analysis of cultured microglia identified TNF-α as a candidate regulator of the response to myelin debris. (A)** Volcano plot of regulated proteins in vehicle-treated *Myd88*$^{-/-}$ versus vehicle-treated WT. **(B)** Volcano plot of regulated proteins in myelin-treated *Myd88*$^{-/-}$ versus myelin-treated WT. The negative $\log_{10}$ transformed P value is plotted against the $\log_2$ transformed LFQ intensity ratios for each protein. Proteins with a P value <0.05 are indicated as red circles, whereas proteins with a P value >0.05 are indicated as blue circles. The hyperbolic curves indicate the threshold of a permutation-based FDR correction for multiple hypotheses (FDR: P = 0.05, s0 = 0.1). **(C)** Heat map of the top 35 regulated proteins, which were consistently quantified in all comparisons. The $\log_2$ fold changes of the proteins are indicated in a color scale from blue to red. **(D)** Heat map of significant upstream regulators predicted by Ingenuity Pathway Analysis. The negative $\log_{10}$ P value was multiplied with the sign of the related z-score. Blue color indicates a decreased activation, whereas red color indicates an increased activation with the corresponding upstream regulator.

observed in patients with aggressive disease (Yeung et al., 2019). These data suggest that inflammation associated with more aggressive disease favors OPC proliferation. Given that pro-inflammatory mediators can induce oligodendrogenesis, it will be important to determine the effects of immune-modulatory or immune-suppressive drugs currently in use to treat MS in remyelination.

Our study also provides evidence for a role of microglia activation in promoting myelin degradation. We found more extensive myelin debris accumulation within microglia in lesioned MyD88-deficient animals than in control. How does MyD88-dependent signaling regulate myelin debris clearance? Previous work analyzing the uptake of bacteria and apoptotic cells in peripheral macrophages provided evidence that TLR-signaling is able to control the mode of phagosome maturation. Engagement of bacteria with TLR receptors was found to alter the kinetics of phagosome maturation by triggering an inducible mode of phagocytosis, resulting in more efficient clearance. The inducible mode is distinguished from a constitutive mode of phagosome maturation by its enhanced phagosome-to-lysosome fusion rate and by the induction of antimicrobial defense systems, such as nicotinamide adenine dinucleotide phosphate oxidase and nitric oxide synthase (Blander and Medzhitov, 2004). Thus, differences in the cellular response that occurs

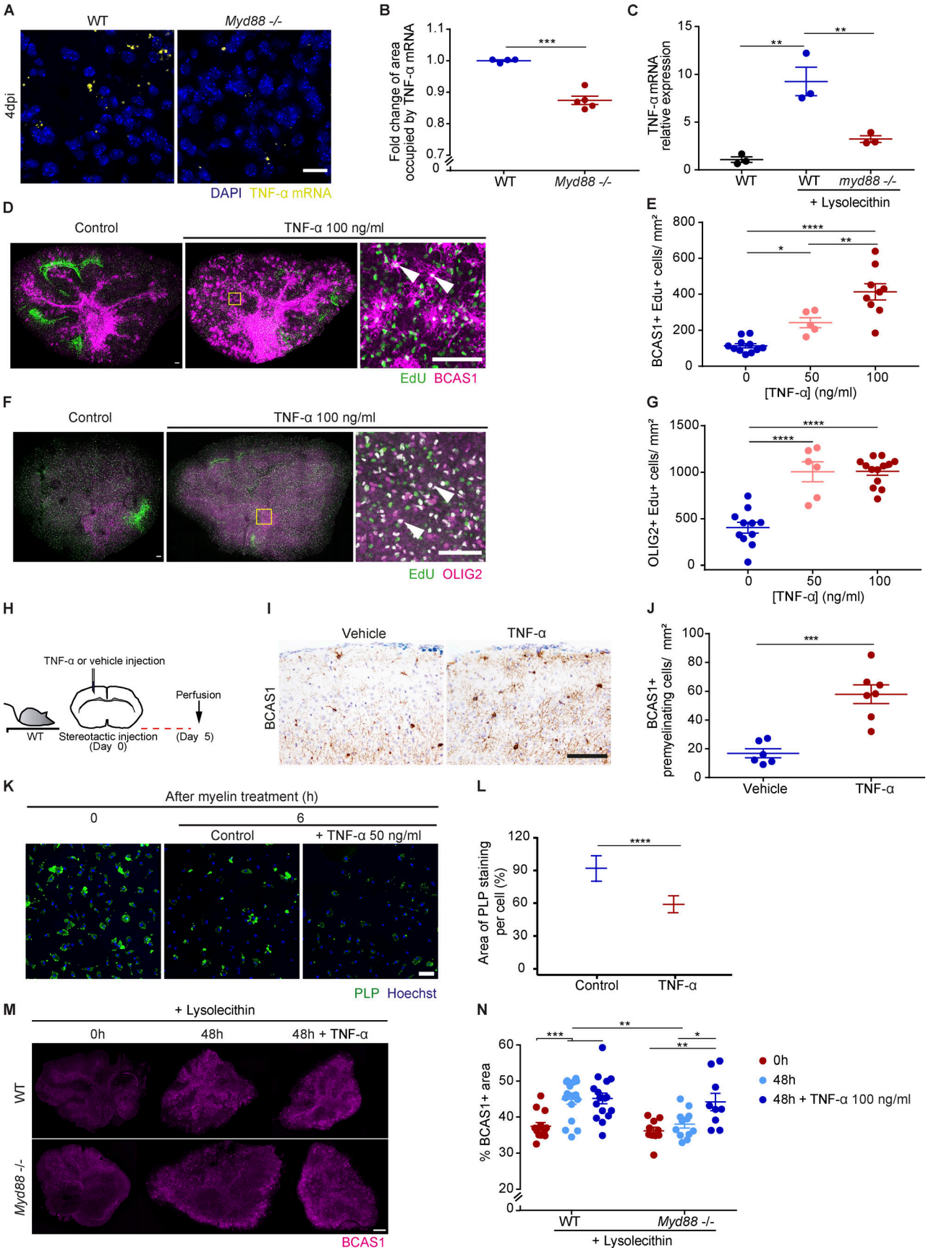

Figure 8. **TNF-α expression is induced after a demyelinating injury and increases the number of premyelinating oligodendrocytes. (A and B)** Confocal maximum intensity z-projections of RNAscope in situ hybridization targeting TNF-α in mouse spinal cord lesions at 4 dpi. TNF-α was determined by the total amount of signal in the lesion. *n* = 4 or 5 lesions. **(C)** TNF-α mRNA in spinal cord lesions of zebrafish larvae was determined by quantitative RT-PCR of lesions at 6 hpi. *n* = 3 independent experiments. **(D–G)** After 5 or 6 DIV, OCSCs were treated with 50 or 100 ng/ml recombinant mouse TNF-α and EdU for 48 h. **(D and E)** Newly formed myelinating oligodendrocytes were labeled by EdU (green) and expressed BCAS1 (magenta; examples of colocalization, white arrowheads) in the cell body. *n* = 5–11 slices in two experiments. **(F and G)** Newly generated oligodendrocytes that expressed OLIG2 (magenta) and incorporated EdU (green; examples of colocalization, white arrowheads). *n* = 6–13 slices in two experiments. **(H)** Schematic representation of cortical injection of TNF-α or vehicle in WT mice. **(I)** IHC of BCAS1 on day 5 after stereotactic injection of vehicle or TNF-α in WT mice. **(J)** Quantification of $BCAS1^+$ cells with a premyelinating morphology in the subpial cortex day 5 after stereotactic injection of vehicle or TNF-α. **(K and L)** 2 h after myelin debris treatment, TNF-α (50 ng/ml) was added to cultured microglia for 6 h. The amount of PLP per cell at 6 h was normalized to the initial amount of PLP per cell (0 h). Myelin treatment control versus TNF-α: P = $3.125 \times 10^{-6}$; effect size (Cohen's *d*) = 0.224; 703 cells in the control group and 1,252 cells in the TNF-α treatment group were sampled randomly. *n* = 3 independent experiments. **(M and N)** After 7 DIV, OCSCs were treated with 0.5 mg/ml LPC for 16 h and subsequently with TNF-α (100 ng/ml) for 48 h, and BCAS1 immunoreactivity was determined in the slices. *n* = 9–17 slices in four to six independent experiments. All data are mean ± SEM (error bars). *, P < 0.05; **, P < 0.01; ***, P < 0.001; ****, P < 0.0001 by unpaired *t* test with Welch's correction in B, J, and L; one-way ANOVA test with Tukey's multiple comparisons test in C, E, and G; and two-way ANOVA test with Tukey's and Sidak's multiple comparisons tests in N. Scale bars: 20 µm in A; 100 µm in D, F, and I; 60 µm in K; and 500 µm in M.

upon uptake of apoptotic and bacterial cargo could be determined by the phagocytic route taken. It is interesting that myelin debris appears to be processed in the system for host defense against infection. The reason why myelin debris employs this route of phagocytosis could lie in its unique structure. Myelin is a multi-layered, tightly packed membrane enriched in lipids that are difficult to break down. Hence, it is possible that microglia activation is required to induce antimicrobial defense for its degradation.

It is important to note that we used a global knockout of MyD88 in the mouse and zebrafish. As a consequence, we do not know whether MyD88-dependent signaling outside of the innate immune system contributed to the phenotype we describe. MyD88 is highly enriched in microglia, although low levels present in oligodendrocytes cannot be excluded, where it can act downstream of pathogen-derived TLR2 agonist–induced signaling to block oligodendrocyte maturation (Sloane et al., 2010). Our study argues that in the absence of such agonists, the pro-inflammatory–mediated induction of OPC proliferation dominates. We provide evidence that generation of TNF-α is triggered in a MyD88-dependent fashion after myelin injury, but it is likely that other pro-inflammatory mediators also contribute to the regenerative response. In the future, it will be important to extend this study to analyze whether inflammatory cytokine signaling–induced OPC stimulation can provide an approach for promoting remyelination. We envision that the novel model of de- and remyelination in the spinal cord of zebrafish larvae established in this work, together with rapid gene targeting, chemical screening, and visualization techniques, will provide a powerful system to identify pathways and small molecules with the potential to enhance regeneration.

## Material and methods

### Zebrafish husbandry

Zebrafish lines were handled according to local animal welfare regulations and kept under standard conditions at the German Center for Neurodegenerative Diseases fish facility in Munich, Germany. Adult zebrafish were mated in individual breeding boxes overnight, and the eggs were collected the morning after in Petri dishes. Fertilized eggs were raised at 28.5°C in E3 medium. For the fish to be raised to adulthood, at 1 dpf, embryos were sorted in clutches of 30 per Petri dish and bleached, followed by addition of pronase to facilitate their hatching. At 5 dpf, larvae were transferred to 3.5-liter tanks in the facility and kept in co-culture with rotifers. After 11 dpf, artemia and powder food were added to their diet. Adult fish were fed artemia and dry food. For the larvae to be used in experiments, 1-phenyl 2-thiourea (Sigma; P7629) was added to the Petri dish at 1 dpf in order to prevent pigmentation; at 5 dpf, larvae were transferred to 600-ml beakers filled with 300 ml of E3 medium, where they started to be fed with powder food once per day until the end of the experiments. The following fish lines were used: Tg(*mpeg1:eGFP*) (Ellett et al., 2011), Tg(*mbp:eGFP-CAAX*) (Almeida et al., 2011), Tg(*mbp:mcherry-CAAX*) (Mensch et al., 2015), Tg(*olig1:nls-mApple*) (Auer et al., 2018), Tg(*mbp:nls-eGFP*) (Karttunen et al., 2017), Tg(*sox10:mRFP*) (Kirby et al., 2006), Tg(*mpeg1:mCherry-F*) (Nguyen-Chi et al., 2014), Tg(*NF-κb:eGFP*) (Ogryzko et al., 2014), *csf1ra*$^{j4e1/j4e1}$; *csf1rb*$^{re01/re01}$ (Oosterhof et al., 2018), and *myd88* $^{hu3568/hu3568}$ (van der Vaart et al., 2013).

### Mouse husbandry

All animal experiments were performed according to German animal welfare law and local regulations for animal experimentation (Regierung von Oberbayern). The genotype of *Myd88*$^{-/-}$ mice (Adachi et al., 1998) was confirmed by genotyping. The DNA fragments were amplified by PCR using the forward primer 5′-GTTGTGTGTGTCCGACCGT-3′ and reverse primer 5′-GTCAGAAACAACCACCACCATGC-3′. The PCR program using GoTaq G2 DNA polymerase (M7845; Promega) was 94°C for 3 min; 35 cycles of 94°C for 30 s, 66°C for 1 min, and 72°C for 1 min; and 72°C for 2 min followed by cooling. The DNA fragments amplified from *Myd88*$^{-/-}$ were 353 bp and 266 bp from WT.

### Zebrafish genotyping

Fin clips from anesthetized 3 mo adult fish or whole larvae were lysed in a solution of Proteinase K (17 mg/ml) and Tris-EDTA buffer for 4 h at 55°C, followed by Proteinase K inactivation at 65°C for 5 min. Genomic DNA was then amplified using the specific primers (*myd88* forward: 5′-GAGGCGATTCCAGTAACAGC-3′, *myd88* reverse: 5′-GAAGCGAACAAAGAAAAGCAA-3′,

*csf1rb* forward: 5′-CTTGCTGACAAATCCAGCAG-3′, and *csf1rb* reverse: 5′-GAGCTAACCGGACAAACTGG-3′), and the product was digested with the appropriate restriction enzymes (MseI for *myd88* and MspI for *csf1rb*) for 2 h. Undigested and digested PCR products were loaded in a 2% gel for gel electrophoresis at 180 V for 50 min. Gels were scanned using a BioRad Gel Doc XR+ system.

### LPC-induced demyelination in the spinal cord of zebrafish larvae

LPC has been applied previously to the adult optic nerve of adult zebrafish (Münzel et al., 2014). Here, we used larvae at 6 dpf anesthetized in E3 medium with tricaine (Pharmaq Limited; MS-222) and placed individually in an agarose mold under a microscope. Larvae were positioned laterally, and the medium was removed as much as possible. A Nanoliter 2010 + Micro4 Controller injection setup was used to perform the injections. Glass needles (World Precision Instruments; 504949) were pulled using a DMZ-Universal puller and fully filled with mineral oil. 2000 nl of oil was infused, and 500 nl of air was withdrawn in order to form an air bubble between the oil and the solution to be injected; right after, 900 nl of a 40% solution of LPC (L-α-lysophosphatidylcholine from egg yolk; Sigma; L4129) in PBS was withdrawn. The setup was set to inject 4 nl at a rate of 23 nl/s, and larvae were injected in the spinal cord at the level of the yolk sac. Immediately after injection, larvae were transferred to a beaker with 300 ml of E3 medium, given powder food, and put back in the incubator (28.5°C). Both concentration and volume to be injected were previously tested.

### In vivo confocal imaging of zebrafish larvae

For live imaging, larvae were anesthetized with tricaine and mounted laterally in 0.8% low melting agarose in E3 medium, using a glass-bottom dish filled with E3 medium and tricaine. Larvae were imaged with a Leica TCS SP8 confocal laser scanning microscope with a climate chamber (28.5°C), using 20 × 0.75 numerical aperture (NA) air or 40 × 1.1 NA water immersion objectives and 488-nm and 552-nm lasers. For the quantification of lysosomes, LysoTracker Red DND-99 dye (Thermo Fisher; L7528) was used by adding 10 µM of the dye to larvae immersed in E3 medium in a 24-well plate. Larvae were incubated for 1 h 30 min in the dark at 28.5°C, followed by four washing steps with fresh E3. After imaging, larvae were removed out of the agarose, sacrificed, and genotyped in case imaged larvae were a result of heterozygous incrosses.

### Image analysis of live imaging experiments in zebrafish larvae

Automated quantification of myelination, phagocyte infiltration, and axons was performed using ImageJ/Fiji software by assessing the total amount of mbp:mCherry-CAAX–, mpeg1:eGFP–, or cntn1b:mCherry–positive pixels, respectively, in a predefined region of interest of maximum intensity projections. Images were thresholded using the Huang method. The final result is expressed as a percentage of the area of the positive signal in the total region of interest. Quantification of NF-κB activation in phagocytes was performed using the three-dimensional surpass view of Imaris software (Bitplane) by generating surfaces of thresholded NF-κB signal and phagocytes. The plug-in Surface-Surface Coloc of Imaris was used to determine the value of co-localization, and the final result was expressed as a percentage of the colocalized surface per total amount of phagocyte surface. The same method was applied to the quantification of lysosomes and myelin inside the phagocytes. The quantification of the number of mature oligodendrocytes or OPCs was performed by manually counting the mbp:nls-eGFP– or olig1:nls-mApple–positive nuclei, respectively, in the dorsal spinal cord in maximum intensity projections. Images were thresholded using the IJ-IsoData method.

### Quantitative RT-PCR of zebrafish lesions

For assessment of the gene expression in lesions, 100 lesions were collected per genotype and snap-frozen in dry ice. RNA was isolated using the RNeasy Mini Kit (Qiagen; 74134) following the QIAshredder dissociation protocol. cDNA was obtained using the SuperScript III First-Strand Synthesis system (Thermo Fisher; 18080051). Quantitative RT-PCR was performed with PowerUP SYBR Green Master Mix (Thermo Fisher; A25780), using a Roche LightCycler 480 Instrument II Real-Time PCR system. The following primers were used: *tnfa* forward: 5′-CTC CATAAGACCCAGGGCAAT-3′, *tnfa* reverse: 5′-ATGGCAGCCTTG GAAGTGAA-3′, *ef1a* forward: 5′-AGCAGCAGCTGAGGAGTGAT-3′, and *ef1a* reverse: 5′-GTGGTGGACTTTCCGGAGT-3′. Samples were run in triplicates, and expression levels were normalized to the housekeeping gene *elf1a*. The ΔΔCt method was used to determine the relative gene expression. Experiments were performed as biological triplicates.

### LPC-induced demyelination in the spinal cord of mice

Stereotactic injection of LPC in the spinal cord was performed in *Myd88*$^{-/-}$ mice that were 9–12 wk old and age-matched WT C57BL/6J mice after at least 2 wk of acclimatization to the animal unit. The reagents for injection were prepared under the cell culture hood. 1% LPC was prepared by dissolving L-α-lysophosphatidylcholine from egg yolk in PBS, pH 7.4 (Gibco; 10010056). 3% Monastral blue was prepared by dissolving Copper (II) phthalocyanine-tetrasulfonic acid tetrasodium salt (Sigma; 274011) in deionized water, and the solution was passed through an 0.45-µm filter and autoclaved. Prior to injection, 1 µl of 3% Monastral blue was mixed with 25 µl of 1% LPC. Glass Capillaries for Nanoliter 2010, fire polished 2 (World Precision Instruments; 504949 or 4878) were pulled using the P-1000 Next Generation Micropipette Puller (Sutter Instrument). The program had the following parameters: Heat 530, Pull 0, Vel 60, Time 250, Pressure 500, Ramp 520, Microinjection–BF100.50.10, Tip <1 µm, Taper 6–8 mm, R ∼40–80 Meg, Heat = Ramp, FB255B, and 2.5 mm Box.

Before surgery, the animals were anesthetized by i.p. injection of 0.5 mg/kg body weight medetomidine, 5.0 mg/kg midazolam, and 0.05 mg/kg fentanyl. The anesthetized animals were kept on a heating pad at 37°C, and Bepanthen eye ointment was applied to prevent drying of eyes. The anesthetic depth was monitored by checking the reflex between the toes and the corneal reflex. The surgery and intraspinal injection of LPC was conducted using the digital mouse stereotaxic frame and

Nanoliter 2010 Injector with MICRO4 controller (World Precision Instruments) as previously described (Cantuti-Castelvetri et al., 2018). After the spinal cord was exposed, the capillary was positioned 0.55 mm lateral to the dorsal artery and lowered 1.15 mm into the tissue. At each injection site, 1 µl of 1% LPC containing 0.12% Monastral blue was injected at a speed of 150 nl/min. 1 min after LPC was delivered, the capillary was slowly retracted. After injection, the skin was sutured, and the wound was disinfected and sealed with the tissue adhesive Histoacryl (B. Braun). After the operation, the animals were injected i.p. with 250 µl of 0.9% NaCl (normal saline solution) to compensate for the loss of blood. The analgesic buprenorphine was injected s.c. at a dose of 0.1 mg/kg. When 0.5 mg/kg body weight medetomidine, 5.0 mg/kg midazolam, and 0.05 mg/kg fentanyl was used for anesthesia, 2.5 mg/kg atipamezole, 0.5 mg/kg flumazenil, and 1.2 mg/kg naloxone was injected i.p. for the animals to wake up. The animals were kept on a heating pad at 37°C until they were awake. They were supplied with wet powder food in a 100-mm Petri dish in addition to regular food and water. The wet powder food was refreshed daily until the animals' hind limbs could function properly. The animals were injected s.c. with buprenorphine 1 or 2 d after surgery.

### Preparation of tissue samples for histology

The mice were fixed by transcardial perfusion to prepare samples for histology. Adult animals were anesthetized by i.p. injection with 100–200 µl of 14% chloral hydrate (prepared in water; Sigma; C8383). The blood was washed out by transcardial perfusion with filtered, ice-cold PBS, pH 7.4, for 5 min until clear liquid came out of the right atrium and the liver turned pale. The animals were then perfused with fresh, filtered, ice-cold 4% paraformaldehyde (PFA) in PBS for 10–15 min until they stiffened. The brain was taken out of the skull and postfixed in 4% PFA at 4°C overnight. The spine was taken out. The bones on the ventral side were removed to expose the ventral spinal cord, and then the spine was fixed in 4% PFA at 4°C for 3–6 d. If only the spinal cord was needed for histology, the mice were anesthetized in a $CO_2$ chamber and euthanized by decapitation. The spine was dissected and fixed in the same way.

After postfixation, the tissue was washed in PBS and processed for cryoprotection. The tissue not required for processing could be stored in PBS containing 0.1% sodium azide at 4°C. The spinal cord was dissected out of the bone. The brain and spinal cord were immersed in 30% sucrose (prepared in PBS on the day of use) at 4°C for 3 d, until the tissue sank to the bottom of the conical tube. The tissue was immersed in 1:1 mixture of 30% sucrose in PBS and Tissue-Tek O.C.T. Compound (Sakura) at room temperature with shaking at 400 rpm overnight. The tissue was transferred to O.C.T. and incubated at room temperature for 4–5 h (spinal cord) or 1 d (brain). Afterward, the tissue was embedded in O.C.T. on dry ice. The frozen tissue was stored at −20°C or −80°C.

Coronal sections of spinal cords and brains were cut at a thickness of 12 µm using a cryostat. The sections were mounted on SuperFrost Plus Microscope Slides (Thermo Fisher; J1800AMNZ). The adjacent spinal cord sections were mounted on alternating slides so that in each pair of slides one slide was used for IHC, whereas the other was used for Luxol Fast Blue stain. The slides were stored at −20°C or −80°C.

### Semi-thin sections

The spinal cord was sectioned coronally using a vibratome (Leica Biosystems) to prepare samples for semi-thin sections. 20% gelatin was prepared by dissolving gelatin powder (Merck Millipore; 1040781000) in PBS by stirring and heating at 60°C. Before vibratome sectioning, the aliquots of 20% gelatin were thawed from −20°C and heated at 37°C with shaking. A segment of spinal cord (shorter than 3 mm) was freshly dissected from the mouse and embedded in 20% gelatin in an embedding mold (Sigma; E4140-1EA) on ice. 200-µm coronal sections were cut at a speed of 0.4–0.5 mm/s. The coronal sections were fixed with a solution containing 4% PFA and 2.5% glutaraldehyde in Karlsson & Schultz buffer, under a coverslip in a 24-well plate at 4°C until further processing. The spinal cord sections were embedded in epon and cut at a thickness of 500 nm using the Leica Ultracut S ultramicrotome. Semi-thin sections were stained with methylene blue-azure II to visualize the lipid-rich areas such as myelin.

### Preparation of myelin and fluorescent labeling

Myelin was isolated from the brains of 12 adult (at least 8-wk-old) WT C57BL/6 mice using the Beckman Optima XL-80 Ultracentrifuge with the SW 28 swinging-bucket rotor. Ultra-Clear Thinwall 38.5-ml tubes (Beckman Coulter; 344058) were sterilized with UV under the laminar hood. The Hepes-EDTA buffer was prepared as 10 mM Hepes and 5 mM EDTA, pH 7.4, filtered, and stored at 4°C. 0.32 M, and 0.85 M sucrose solutions were prepared freshly in cold 10 mM Hepes, pH 7.4 (Hepes buffer), and filtered. Deionized water was also filtered and kept cold. The mice were euthanized in a $CO_2$ chamber followed by decapitation. Three or four brains were put in a Dounce homogenizer containing 4 ml of Hepes buffer. The brains were first homogenized mechanically using the Dounce tissue grinder set. The homogenate was transferred to a conical tube and topped up to 5 ml with Hepes buffer. The homogenate was then sonicated for 5 min using the Sonifier W-250 D (Branson). The brain homogenate was stored at −20°C.

The isolation and purification of myelin were done at 4°C or on ice. 5 ml of brain homogenate was overlaid on a stepwise 0.32/0.85 M sucrose gradient in an ultracentrifugation tube. The first centrifugation was done at 23,800 rpm (54,000 ×*g*) for 35 min. The myelin fraction was collected from the interphase using a P1000 pipette. Deionized water was added to the myelin to remove small membrane fragments by osmotic shock. Myelin was pelleted by centrifugation at 23,800 rpm (54,000 ×*g*) for 18 min. The supernatant was aspirated carefully, and the pellets were resuspended with water. Myelin was washed with water and centrifuged at 9,500 rpm (9,000 ×*g*) twice for 18–22 min. The supernatant was removed; 1 ml of Hepes buffer was added to each pellet, and the pellets were kept at −20°C until the purification steps. The crude products of myelin were purified by repeating the stepwise density gradient centrifugation, osmotic shock, and two washing steps. The Hepes buffer for cell culture was prepared from the 1 M Hepes (Gibco; 15630056), and the pH was measured by pH-indicator strips (Merck Millipore; 109543)

and adjusted to 7.4 with sodium bicarbonate 7.5% solution (Thermo Fisher; 25080). Each final pellet was resuspended with 500 µl of Hepes buffer for cell culture. The myelin was passed through a syringe attached to a 27G cannula. The concentration of proteins in myelin was measured by Bradford assay.

Purified myelin was labeled using the PKH67 Green Fluorescent Cell Linker Mini Kit (Sigma; MINI67) for use in live-cell imaging. For each 200–300 µg myelin in 250 µl Hepes buffer for cell culture, a mixture of 750 µl of Diluent C and 4 µl of PKH67 (vortexed for mixing) was added. The mixture was incubated for 5 min at room temperature (protected from light) and centrifuged at 15,000 ×*g* for 10 min at 4°C. The pellet was resuspended with 250 µl of Hepes buffer or PBS for cell culture and passed through a 27G cannula.

### Microglial cell culture

Primary microglial cells were isolated by magnetic-activated cell sorting (MACS). Microglia were cultivated in the DMEM/FCS/L929 medium until the cells were ready for experiment. The MACS microglia cultures were washed and incubated with the serum-free TGF-β/CSF-1/cholesterol (TCC; or TGF-β/Il-34/cholesterol [TIC]) medium for 3 h to overnight before experiment (Bohlen et al., 2017). To improve the attachment of cells, No. 1.5 coverslips were treated with hydrochloric acid (fuming) overnight, washed at least 10 times with distilled water, dried, and disinfected at 200°C for 6 h. Glass coverslips were coated with 0.01% poly-L-lysine for 1 h at 37°C and washed twice with PBS for 5 min for microglia culture. Growth of microglia in plastic plates did not require any coating. The conditioned medium of the L929 cell line contains factors such as M-CSF that stimulate the growth of microglia and macrophages. L929 cells were cultured in DMEM/FCS medium. The medium was renewed every 2 or 3 d. L929 cells were split at a sub-cultivation ratio of 1:2 to 1:8 three times to obtain cultures in 10 175-$cm^2$ flasks. The medium was conditioned with confluent L929 cultures for 10–14 d. L929 cell–conditioned medium was collected and passed through a 0.22-µm filter.

MACS microglial cell cultures were prepared from the brains of postnatal day (P)9–P10 mouse pups, when the number of microglia was high and the dissociation of brain tissue was relatively easy. P6–P8 brains yielded fewer, but a sufficient number of, cells. Cell suspension was obtained by automated dissociation using the Neural Tissue Dissociation Kit (P; Miltenyi Biotec; 130–092-628) and the gentleMACS Dissociator (Miltenyi Biotec; 130–093-235) following the datasheet of the kit with some modifications. Two or three brains were transferred to each C Tube (Miltenyi Biotec; 130–096-334). DMEM/pyruvate medium was used instead of HBSS during tissue dissociation. All media were warmed up to room temperature. The gentleMACS programs for the brain were run twice per tube. The optional centrifugation steps were included in the protocol. For the filtering of cell suspension through 70-µm cell strainers (Corning; 352350), 5 ml of cell suspension was applied to one cell strainer and washed with 5 ml of DMEM/pyruvate medium. After filtration, the cell suspension was centrifuged at 300 ×*g* for 15 or 20 min. The cells were resuspended and topped up to 20 ml, and the sample was diluted 1/10 for counting the cell number using a hemocytometer. The cell suspension was centrifuged again at 300 ×*g* for 15 or 20 min. The myelin removal step was omitted. Microglia were isolated by magnetic labeling with CD11b MicroBeads (Miltenyi Biotec; 130–093-634). DMEM/FCS medium instead of the buffer was used, and the serum was needed to block nonspecific binding. After the incubation with beads on ice, the cells were washed with 2 ml of DMEM/FCS medium per 107 cells and centrifuged at 300 ×*g* for 12–15 min at 4°C. The pellet was resuspended in 500 µl of DMEM/FCS medium per 107 cells. $CD11b^+$ cells were separated from the other cells in LS columns (Miltenyi Biotec; 130–042-401) and QuadroMACS Separator (Miltenyi Biotec). After magnetic separation, $CD11b^+$ cells were flushed out in DMEM/FCS/L929 medium. The cells were counted, diluted to the desired density and volume in DMEM/FCS/L929 medium, and seeded in multiple-well plates or 8-well µ-slides. The cultures were maintained under standard cell culture conditions at 37°C with 5% $CO_2$.

To detect oxidative activity, microglia cultures were incubated with DMEM/pyruvate containing 50 µg/ml OxyBURST Green H2HFF BSA (Invitrogen; O-13291), 5 µg/ml Hoechst 33342 (Invitrogen; H3570), and 0.5 µg/ml cholera toxin subunit B (CT-B) Alexa Fluor 647 conjugate (Invitrogen; C34778) for 30 min. The cells were treated with 8 µg/ml myelin (or Hepes vehicle control) in DMEM/pyruvate for 2 h. After treatment, the cells were fixed, immunostained for PLP, and analyzed by confocal microscopy.

For live-cell imaging, microglia isolated by MACS were seeded in poly-L-lysine–coated µ-slides 8-well ibiTreat (ibidi; 80826). The cells were cultured in DMEM/FCS/L929 medium to 90% confluency for 4–7 d, washed twice with DMEM/pyruvate to remove residual serum, and then incubated with serum-free TCC medium overnight. The TCC/Hepes/FluoroBrite medium was used for live-cell imaging experiments. FluoroBrite DMEM is a clear medium with low background fluorescence. The medium was supplemented with 20 mM Hepes to maintain pH 7.4 (as in the Live Cell Imaging Solution; Invitrogen; A14291DJ). Before treatment, the cell membrane and nuclei were prelabeled by the incubation with CT-B Alexa Fluor 647 conjugate and Hoechst 33342 for 15 min. Microglia cultures were treated with 30 µg/ml PKH67-labeled myelin (pulse) and 40 nM LysoTracker Red DND-99 (Invitrogen; L7528) for 15 min. After treatment, the medium was changed to TCC/Hepes/FluoroBrite, and the cells were incubated for 60 min (chase) before imaging. The prelabeling of the cell membrane with CT-B could minimize nonspecific binding of CT-B to the myelin membrane. LysoTracker was used before the chase to preserve the signal and avoid the accumulation of excessive LysoTracker inside cells.

To analyze the clearance of myelin debris, microglia cultures were treated with 8 µg/ml myelin (or Hepes control) in the TCC medium for 2 h. After treatment, the cells were washed three times and incubated with the TCC medium for 6 or 24 h. After fixation, the myelin in cells was stained using FluoroMyelin Green or anti-PLP antibody; the cells were stained using DyLight 694–labeled tomato lectin (Vector Laboratories; DL-1178) and 2 µg/ml Hoechst 33342.

### OCSC

OCSCs were prepared as previously described (Hill et al., 2014). The cultures were prepared from the brains of P6–P8 C57BL/6J

mouse pups. Cerebellar slices were cultured on small pieces of LCR membrane filter (Merck Millipore; FHLC04700) placed on Millicell cell culture inserts (Merck Millipore; PICM03050). LCR membrane was put in a big glass dish, wet with deionized water, flattened, air-dried, and then cut into small pieces of ∼5 mm × 6 mm using a scalpel. The confetti LCR membrane was autoclaved in the dish. In a 6-well plate, 0.7 ml of OCSC medium was pipetted in each well. Cell culture inserts were placed in the wells, and five or six pieces of confetti LCR membrane were placed carefully on each insert (bubbles should be avoided). The plates were conditioned in the cell culture incubator for at least 2 h. Dissection buffer was kept at 4°C. The MCILWAIN Tissue Chopper, stereomicroscope, and dissection tools were disinfected with 70% ethanol and UV under a laminar hood. The brain was dissected out and transferred immediately to ice-cold dissection buffer in a 60-mm culture dish placed on ice. The cerebellum was dissected out under the stereomicroscope and transferred to the platform of the tissue chopper with a cut transfer pipette (Thermo Fisher; 232-1S). The liquid was removed from the stage with a transfer pipette with a fine tip. The platform was rotated and fixed to place the cerebellum perpendicular to the blade. After cutting at 300 µm, the slices were transferred with a cut transfer pipette to a dish containing dissection buffer on ice. The intact cerebellar slices were selected and transferred to confetti LCR membrane in the plate. OCSC was maintained at 37°C with 5% $CO_2$. The culture medium was changed the day after culture preparation and then every 2 or 3 d. After 5 or 6 d in vitro (DIV), OCSCs were recovered from the culture preparation and were ready for experiments. Cell proliferation was labeled with 10 µM EdU. OCSC was treated with recombinant mouse TNF-α (aa 80–235) protein (R&D Systems; 410-MT-025/CF) in 50% OCSC medium for 48 h.

For the induction of demyelination in OCSC, P8–P9 mouse pups C57BL/6J (WT) or *Myd88*$^{-/-}$ were decapitated with one clean cut using scissors. The brain was dissected, and the cerebellum was transferred to ice-cold HBSS (with calcium and magnesium). Using the McIlwain Tissue Chopper, the cerebella were cut into 300-µm sagittal slices and immediately transferred to ice-cold dissection media (1× HBSS with calcium and magnesium [Gibco], 15 mM Hepes [Gibco], and 0.57% glucose 45% [Sigma]). The individual slices were separated, and up to four slices were placed in the same insert. 6-well plates with 0.4 µM, 30-mm diameter cell culture inserts, and 1 ml of culture media (50% MEM 10× no glutamine and with Earle's salts, 5% BME with Earle's salts, 25% horse serum, 1× GlutaMAX 100× [Gibco], 0.648% glucose 45%, 0.5% Penicillin/Streptomycin, 7.5% $NaHCO_3$ to adjust the pH to ∼7.2, and autoclaved deionized water) were previously prepared and put in the incubator (at 37°C, 5% $CO_2$) for at least 2 h before placing the slices, for acclimatization of the insert membranes and oxygenation of the media. The medium was changed 1 d after the culture was prepared and then every 3 d. Demyelination of the slices was induced as previously described (Thetiot et al., 2019). Briefly, at 7 DIV the inserts containing the cerebellar slices were placed in fresh medium containing 0.5 mg/ml LPC (L-alfa-lysophosphatidylcholine from egg yolk) in PBS for 16 h in the incubator. Afterward, the slices were either washed with PBS and fixed in 4% PFA or changed to fresh medium and placed back in the incubator for the remaining time of the experiment.

### IHC

IHC of lesions was conducted on mounted spinal cord sections. To facilitate the attachment of mounted cryosections to the slides, the slides were dried in a 37°C incubator for 30 min (or at room temperature for at least 1 h) and washed twice with PBS for 5 min. A circle was drawn around each section with a Super PAP Pen Liquid Blocker Mini (Science Services; N71312) for incubation with solution. For the IHC for cytoplasmic proteins, the sections were blocked and permeabilized with blocking solution (2.5% bovine serum, 2.5% BSA, and 2.5% fish gelatin in PBS) containing 0.1% Triton X-100 for 1 h at room temperature. The sections were incubated with primary antibodies in blocking solution containing 0.1% Triton X-100 overnight at 4°C (one section incubated without primary antibodies as a control for the specificity of secondary antibodies), and washed three times with PBS for 10 min. The sections were then incubated with secondary antibodies in blocking solution containing 0.1% Triton X-100 for 1–2 h at room temperature, followed by a wash with PBS for 10 min. Mild permeabilization using 0.1% Triton X-100 was required for FluoroMyelin stain. After the incubation with secondary antibodies, the sections were incubated with 1:350 FluoroMyelin Green Fluorescent Myelin Stain (Molecular Probes; F34651) in PBS for 20 min at room temperature. The nuclei were stained with 1 µg/ml 4′,6-diamidino-2-phenylindole (DAPI) or 2 µg/ml Hoechst 33342 in PBS for 15–30 min at room temperature. The sections were washed twice with PBS for 10 min, mounted with Mowiol or ProLong Diamond Antifade Mountant (Thermo Fisher; P36970) and #1.5 coverslip, and air-dried overnight.

The IHC for OLIG2, NKX-2.2, and APC (CC1) required heat-induced antigen retrieval in 10 mM sodium citrate, pH 6.0. The sections were heated using the 120°C autoclaving program for liquids. After cooling down, the sections were washed twice with PBS for 10 min and permeabilized with blocking solution containing 0.3% Triton X-100 for 1 h at room temperature. The sections were incubated with primary antibodies in blocking solution containing 0.1% Triton X-100 for 2 d at 4°C; this longer incubation allows optimal staining of all oligodendrocyte-lineage cells with the anti-OLIG2 antibody. After washing, the sections were incubated with secondary antibodies in blocking solution containing 0.1% Triton X-100 for 2 h at room temperature, and the other procedures were the same as for cytoplasmic antigens. The primary antibodies used were anti-APC (Ab-7) mouse mAb (CC1; 1:100; Calbiochem; OP80), NABC1 (BCAS1) antibody (5) mouse monoclonal IgG1 κ (1:250; Santa Cruz; sc-136342), anti-IBA1 polyclonal antibodies, rabbit (1:500; Wako, 019–19741), Nkx2.2 mouse hybridoma, clone 74.5A5 (1:5; Developmental Studies Hybridoma Bank, University of Iowa), and anti–Olig-2 rabbit polyclonal antibody (1:250; Chemicon; AB9610). The following secondary antibodies used were goat anti-rabbit IgG (H+L) cross-adsorbed secondary antibody, Alexa Fluor 647 (1:1,000–1:750; Thermo Fisher; A-21244), goat anti-rabbit IgG (H+L) cross-adsorbed secondary antibody, Alexa Fluor 555 (1:1,000; Thermo Fisher; A-21428), goat anti-rabbit IgG (H+L)

cross-adsorbed secondary antibody, Alexa Fluor 488 (1:1,000; Thermo Fisher; A-11008), goat anti-rat IgG (H+L) cross-adsorbed secondary antibody, Alexa Fluor 488 (1:1,000–1:750; Thermo Fisher; A-11006), goat anti-mouse IgG (H+L) cross-adsorbed secondary antibody, Alexa Fluor 647 (1:1,000; Thermo Fisher; A-21235), and goat anti-mouse IgG (H+L) cross-adsorbed secondary antibody, Alexa Fluor 555 (1:1,000–1:750; Thermo Fisher; A-21422).

The IHCs of cultured organotypic cerebellar slices were performed as a free-floating protocol with the slices on the membrane. The slices were washed three times with warm PBS, fixed with 4% PFA in PBS for 2 h at room temperature, and washed three times with PBS for 5 min with mild shaking. The IHC for BCAS1 requires mild permeabilization. The slices were blocked and permeabilized with blocking solution containing 0.1% saponin and 0.02% sodium azide (block/saponin/$NaN_3$) for 2 h at room temperature with mild shaking and incubated with primary antibodies in block/saponin/$NaN_3$ for 1 d at 37°C with shaking. The slices were washed six times with PBS for 30 min at room temperature, incubated with secondary antibodies in block/saponin/$NaN_3$ overnight at 37°C, and then washed three times with PBS for 30 min at room temperature. The IHC for OLIG2 requires heat-induced antigen retrieval as described for spinal cord sections. After washes, the slices were incubated with blocking solution containing 0.5% Triton X-100 and 0.02% sodium azide during blocking/permeabilization and antibody incubation steps. Afterward, EdU was detected using the Click-iT EdU Alexa Fluor 488 imaging kit (Thermo Fisher; C10337). The slices were incubated with blocking solution for 10 min at room temperature and Click-iT reaction cocktail for 45 min and then washed with blocking solution and PBS for 10 min each. The nuclei were stained with 1 µg/ml DAPI or 2 µg/ml Hoechst 33342 in PBS for 30 min at room temperature. After two washes with PBS for 30 min, the slices on the membrane were mounted on SuperFrost Plus slides with mounting medium and #1.5 coverslip.

### Immunocytochemistry

The cells cultured on coverslips were washed with warm PBS, fixed with 4% PFA in PBS for 10–15 min at room temperature, and washed three times with PBS for 5 min. To analyze the amount of myelin in microglia, the cells were incubated with blocking solution containing 0.05% saponin for mild permeabilization. After blocking, the cells were incubated with primary antibody in block/0.05% saponin for 1 h, washed three times with PBS for 5 min, incubated with secondary antibodies and/or lectin in block/0.05% saponin for 45 min to 1 h, and washed with PBS for 5 min. After immunocytochemistry, FluoroMyelin stain in PBS was incubated with the cells for 20 min followed by a wash with PBS. After the counterstain with 1 µg/ml DAPI or 2 µg/ml Hoechst 33342 in PBS for 15 min at room temperature, the coverslips were washed twice with PBS and once with distilled water, dried quickly, and mounted on slides. The primary antibody used was mouse anti-myelin proteolipid protein (clone plpc1) IgG2a mAb (1:200; Bio-Rad; MCA839G). The secondary antibodies used were goat anti-mouse IgG (H+L) cross-adsorbed secondary antibody, Alexa Fluor 555 (1:750), DyLight 649–labeled *Lycopersicon esculentum* (tomato) lectin (1:200; Vector Laboratories; DL-1178, 1177, or 1174), and FluoroMyelin Green Fluorescent Myelin Stain (1:350).

### Imaging, analysis, and statistics of mouse lesions and cell culture experiments

The fluorescent images of spinal cord lesions and the images of immunocytochemistry were acquired using a Leica DMI6000 widefield microscope (20 × 0.4 NA air objective), a Leica SP5 confocal microscope (20 × 0.75 NA air or 63 × 1.4 NA oil objective), or a Nikon C2+ confocal microscope (10 × 0.4 NA air or 60 × 1.4 NA oil objective). Live-cell imaging was conducted using the Leica SP5 confocal microscope (10 × 0.4 NA air objective). The images of OCSCs were acquired using the Nikon C2+ or Leica TCS SP8 confocal laser scanning microscopes (10× objective). The bright-field images of semi-thin sections were acquired using the Leica DMI6000 widefield microscope using the 440 × 0.6 NA air objective. The bright-field images of LFB(-PAS) stain of spinal cord sections were acquired as tile scans using a Zeiss Axiophot microscope, an Olympus BX61VS light microscope, or a Zeiss Axio Imager M2 using the 20× objective. The fluorescent images were analyzed using the software Fiji (Schindelin et al., 2012). Automated cell counting and measurement were conducted using CellProfiler (Carpenter et al., 2006). The data were plotted and statistical tests were performed using the software Graphpad Prism. The csv spreadsheets containing the data of individual cells were analyzed using R and RStudio. The data were visualized using the package ggplot2.

### Proteomics and pathway analysis of cultured microglia

Microglia isolated by MACS from WT and *Myd88*$^{-/-}$ mouse pups were seeded at a density of 1 × $10^6$ cells per 60-mm dish in DMEM/FCS/L929 medium. After 2 DIV, microglia were washed with warm DMEM/pyruvate medium and treated with 20 µg/ml myelin debris (or Hepes control) in 2 ml of TIC medium for 4 h. After treatment, the cells were washed with DMEM/pyruvate medium and incubated with 4 ml of DMEM containing 0.2% BSA for 16 h. The cells in each dish were washed with 2 ml of cold PBS on ice and lysed with 200 µl of cell lysis buffer (Cell Signaling Technology; 9803) containing 1 mM PMSF for 5 min on ice. The cells were detached using cell scrapers, collected, and stored at −80°C. The mass spectrometry label-free quantification (LFQ) was performed for the cell lysate of cultured microglia (triplicates or quadruplicates of each condition). The proteomic data were analyzed using MaxQuant and Ingenuity Pathway Analysis.

A protein amount of 15 µg of each cell lysate was subjected to proteolytic digestion with 0.3 µg LysC (Promega) and 0.15 µg trypsin (Promega) using the filter-assisted sample preparation protocol (Wiśniewski et al., 2009) with 30-kD Vivacon spin filters (Sartorius). Proteolytic peptides were desalted by stop and go extraction with C18 tips (Rappsilber et al., 2003). The purified peptides were dried by vacuum centrifugation. Samples were dissolved in 20 µl 0.1% formic acid. Peptides were analyzed on an Easy nLC 1200 nanoHPLC (Thermo Fisher), which was coupled online via a Nanospray Flex Ion Source (Thermo Fisher)

equipped with a PRSO-V1 column oven (Sonation) to a Q-Exactive High Field mass spectrometer (Thermo Fisher). An amount of 1.3 µg of peptides was separated on an in-house packed C18 column (30 cm × 75 µm inner diameter; ReproSil-Pur 120 C18-AQ, 1.9 µm; Dr. Maisch GmbH) using a binary gradient of water (A) and acetonitrile (B) supplemented with 0.1% formic acid (0 min, 2% B; 3:30 min, 5% B; 137:30 min, 25% B; 168:30 min, 35% B; 182:30 min, 60% B) at 50°C column temperature with a flow rate of 250 nl/min. A data-dependent acquisition method was used. Full mass spectrum scans were acquired at a resolution of 120,000 (m/z range: 300–1,400, automated gain control target: 3E+6). The 15 most intense peptide ions per full mass spectrum scan were selected for peptide fragmentation (resolution: 15,000; isolation width: 1.6 m/z; and AGC target: 1E+5, normalized collision energy: 26%). A dynamic exclusion of 120 s was used for peptide fragmentation.

The data were analyzed with the software Maxquant (https://maxquant.org, Max-Planck Institute Munich) version 1.6.1.0 (Cox et al., 2014). The mass spectrometry data were searched against a reviewed canonical fasta database of *Mus musculus* from UniProt (download: January 17, 2018; 16,954 entries). Trypsin was defined as protease. Two missed cleavages were allowed for the database search. The option first search was used to recalibrate the peptide masses within a window of 20 ppm. For the main search, peptide and peptide fragment mass tolerances were set to 4.5 and 20 ppm, respectively. Carbamidomethylation of cysteine was defined as static modification. Acetylation of the protein N-term as well as oxidation of methionine were set as variable modifications. The FDR for both peptides and proteins was adjusted to <1%. LFQ of proteins required at least two ratio counts of unique peptides. Only unique peptides were used for quantification. The software Perseus (version 1.5.8.5) was used for further data analysis (Tyanova et al., 2016). The protein LFQ intensities were $\log_2$ transformed, and a two-sided Student's *t* test was applied to evaluate the significance of proteins with changed abundance. Additionally, a permutation-based FDR estimation was used (Tusher et al., 2001). Furthermore, Ingenuity Pathway Analysis was performed with default settings using a $\log_2$ fold change larger than ±0.5 and a P value <0.05 as thresholds for protein regulation.

### Scanning electron microscopy

Zebrafish larvae instant fixation in 2.5% glutaraldehyde (electron microscopy grade; Science Services) and 2 mM calcium chloride in 0.05 M sodium cacodylate buffer at pH 7.4 was achieved in a BioWave microwave (Pelco; 100 W, 450 W, five cycles) and preceded an incubation at 4°C for 24–48 h (Czopka and Lyons, 2011). Mouse spinal cord samples were dissected, shortly immersion fixed in 2% PFA (EM grade), 2.5% glutaraldehyde, and 2 mM calcium chloride in 0.1 M sodium cacodylate buffer at pH 7.4, mounted in 20% gelatin for vibratome sectioning in 0.1 M PBS, and fixed for another 24–48 h at 4°C. The BioWave microwave was used for further EM processing using the Hua et al. (2015) protocol. Fish and mouse tissue were postfixed in 2% osmium tetroxide (Science Services) and 2 mM calcium chloride in 0.1 M (mouse) and 0.05 M (fish) sodium cacodylate, followed by a reducing step in 2.5% potassium hexacyanoferrate (Sigma). After thiocarbohydrazide (1% in water; Sigma) incubation, the tissue was further contrasted by 2% aqueous osmium and overnight incubation in 1% uranyl acetate (EMS). Samples were dehydrated at increasing ethanol concentrations and embedded in LX112. For scanning electron microscopy imaging, 100-nm-thin sections (Leica UC7 ultramicrotome) were adsorbed onto carbon nanotube tape strips (Science Services; Kubota et al., 2018). Lesions in zebrafish larvae were relocated according to anatomical landmarks. The tissue was trimmed in 50-µm steps, and ultrathin sections were taken to screen for the lesion site. Scanning electron microscopy imaging for mouse and zebrafish spinal cord samples was performed on a Crossbeam 340 (Zeiss). Images were taken at 10 ×10 × 100 nm and analyzed using ImageJ/TrakEM2 (Cardona et al., 2012).

### In situ hybridization using RNAscope

Detection of TNF-α mRNA in mouse tissue sections was performed using the commercially available RNAscope Multiplex Fluorescent Reagent Kit (v2; Advanced Cell Diagnostics), following manufacturer's instructions. Briefly, 12-µm tissue sections containing lesions were mounted onto SuperFrost Plus slides (Thermo Fisher). The sections were treated with hydrogen peroxide followed by target retrieval. Afterward, the sections were incubated with protease III for 30 min at 40°C. Probe hybridization (TNF-α probe 1:50) was performed for 2 h at 40°C, followed by a series of signal amplification and washing steps. Fluorescent in situ hybridization signals were developed using the Opal 570 fluorophore (1:2,000). Sections were counterstained with DAPI for 30 s at room temperature, and the slides were mounted with the provided ProLong Gold Antifade Mountant. RNA integrity and assay success were controlled by using a probe specific to the housekeeping gene cyclophilin B (PPIB). Negative control background staining was assessed by using a probe specific to the bacterial gene dapB. Sections were imaged with a Leica TCS SP8 confocal laser scanning microscope using 40× water immersion objective and 405-nm and 552-nm lasers. Automated TNF-α mRNA quantification in mice lesions was performed using ImageJ/Fiji software by quantifying the total area occupied by positive pixels in the whole field of view of manually thresholded maximum intensity projections.

### Intracerebral stereotactic injections of TNF-α

Mice were anaesthetized by intraperitoneal injection of ketamine/xylazine and mounted on a stereotactic device (Stoelting Co.). The scalp was opened, and a fine hole was drilled into the skull 0.1 mm caudal to the bregma and 0.2 mm lateral to the sagittal suture. A finely calibrated glass capillary was inserted into the cortex to a depth of 0.7 mm. 60 ng TNF-α (R&D Systems) diluted in PBS was carefully injected in a volume of 2 µl, while controls received PBS only. To identify the injection site, Monastral blue (Sigma-Aldrich) was added to the mixture. After injection, the glass capillary was withdrawn and the scalp was closed by suture.

### Statistical analysis

Statistics were performed using GraphPad Prism7 or R and are specified in each figure legend according to experiments. All

data were tested for normality. One-way ANOVA or two-way ANOVA, with Tukey's or Sidak's multiple comparisons test, Kruskal-Wallis test with Dunn's multiple comparisons test, and unpaired *t* test with Welch's correction were used as appropriate to each experiment. *, P < 0.05; **, P < 0.01; ***, P < 0.001; and ****, P < 0.0001; n.s. indicates no significance. All data are presented as mean ± SEM and *n* = number of animals, unless stated otherwise in the figure legends. The effect sizes were calculated for cell culture experiments, in which individual cells were analyzed using the following formula:

$$d = \frac{M_{group1} - M_{group2}}{SD_{pooled}}$$

$$SD_{pooled} = \sqrt{\frac{SD_{group1}{}^2 + SD_{group2}{}^2}{2}}$$

### Data availability

Further information and data that support the findings of this study are available from the corresponding author upon reasonable request. The accession no. for the proteomics data reported in this paper is PXD014625, and the datasets are available in the ProteomeXchange Consortium via the PRIDE partner repository (Perez-Riverol et al., 2019).

### Online supplemental material

Fig. S1 shows the characterization of WT and *Myd88*$^{-/-}$ zebrafish and mice in noninjected and injected conditions. Fig. S2 shows that myelination and phagocyte infiltration are not affected in *myd88*$^{-/-}$ noninjected larvae. Fig. S3 shows that developmental and adult oligodendrogenesis is not affected in MyD88-deficient mice. Fig. S4 displays the proteome analysis of cultured microglia. Fig. S5 shows the quantification of TNF-α in IBA1$^{+}$ cells. Video 1 shows phagocytes in a demyelinating lesion in WT zebrafish larvae at 2 dpi. Video 2 depicts phagocytes in a demyelinating lesion in WT zebrafish larvae at 3 dpi. Video 3 shows phagocytes in a demyelinating lesion in *myd88*$^{-/-}$ zebrafish larvae at 3 dpi. Table S1 lists the up-regulated proteins induced by myelin debris in cultured WT and *Myd88*$^{-/-}$ microglia. Table S2 lists the up-regulated proteins induced by myelin debris in cultured WT microglia. Table S3 shows the number of total regulated proteins from proteomics.

## Acknowledgments

We thank Alexander Hruscha for technical advice. We thank Alexandra Graupner, Herma van der Linde, and the animal caretakers of the respective animal facilities for mouse and fish care. We thank Uwe-Karsten Hanisch and Arthur Liesz (Institute for Stroke and Dementia Research, Munich, Germany) for providing the *Myd88*$^{-/-}$ mouse line. We thank Tim Czopka (Institute of Neuronal Cell Biology, Technical University of Munich, Munich, Germany), Michell Reimer (DFG-Center for Regenerative Therapies Dresden, Technical University of Dresden, Dresden, Germany), and David Lyons (Centre for Neuroregeneration, University of Edinburgh, Edinburgh, UK) for providing zebrafish lines.

The work was supported by grants from the German Research Foundation (STA 1389/2-1, TRR128, TRR 274, SyNergy Excellence Cluster, EXC 2145, project ID 390857198), European Research Council (Consolidator Grants to M. Simons), the Dr. Miriam and Sheldon G. Adelson Medical Research Foundation, the German Multiple Sclerosis Society (to C. Stadelmann), and the National Multiple Sclerosis Society (to C. Stadelmann). M.I. Cunha was supported by a Fundação para a Ciência e Tecnologia PhD fellowship (PD/BD/105749/2014).

Author contributions: M.I. Cunha, M. Su, and M. Simons conceived the project and designed experiments. M.I. Cunha, M. Su., I. Alexopoulos, S.A. Müller, L. Cantuti-Castelvetri, F. van der Meer, A. Winkler, and M. Schifferer carried out experiments. M.I. Cunha, M. Su, S.A, Müller, L. Cantuti-Castelvetri, I. Alexopoulos, F. van der Meer, T.J. van Ham, B. Schmid, S.F. Lichtenthaler, C. Stadelmann, M. Djannatian, and M. Simons analyzed the data or supervised data acquisition. M.I. Cunha, M. Su, and S.A. Müller visualized the data. M. Simons supervised the project and wrote the manuscript.

Disclosures: The authors declare no competing interests exist.

Submitted: 28 July 2019
Revised: 22 November 2019
Accepted: 17 January 2020

## References

Adachi, O., T. Kawai, K. Takeda, M. Matsumoto, H. Tsutsui, M. Sakagami, K. Nakanishi, and S. Akira. 1998. Targeted disruption of the MyD88 gene results in loss of IL-1- and IL-18-mediated function. *Immunity.* 9: 143–150. https://doi.org/10.1016/S1074-7613(00)80596-8

Akassoglou, K., J. Bauer, G. Kassiotis, M. Pasparakis, H. Lassmann, G. Kollias, and L. Probert. 1998. Oligodendrocyte apoptosis and primary demyelination induced by local TNF/p55TNF receptor signaling in the central nervous system of transgenic mice: models for multiple sclerosis with primary oligodendrogliopathy. *Am. J. Pathol.* 153:801–813. https://doi.org/10.1016/S0002-9440(10)65622-2

Almeida, R.G., T. Czopka, C. Ffrench-Constant, and D.A. Lyons. 2011. Individual axons regulate the myelinating potential of single oligodendrocytes in vivo. *Development.* 138:4443–4450. https://doi.org/10.1242/dev.071001

Arnett, H.A., J. Mason, M. Marino, K. Suzuki, G.K. Matsushima, and J.P. Ting. 2001. TNF alpha promotes proliferation of oligodendrocyte progenitors and remyelination. *Nat. Neurosci.* 4:1116–1122. https://doi.org/10.1038/nn738

Auer, F., S. Vagionitis, and T. Czopka. 2018. Evidence for Myelin Sheath Remodeling in the CNS Revealed by In Vivo Imaging. *Curr. Biol.* 28: 549–559.e3. https://doi.org/10.1016/j.cub.2018.01.017

Birgbauer, E., T.S. Rao, and M. Webb. 2004. Lysolecithin induces demyelination in vitro in a cerebellar slice culture system. *J. Neurosci. Res.* 78: 157–166. https://doi.org/10.1002/jnr.20248

Blander, J.M., and R. Medzhitov. 2004. Regulation of phagosome maturation by signals from toll-like receptors. *Science.* 304:1014–1018. https://doi.org/10.1126/science.1096158

Block, M.L., L. Zecca, and J.S. Hong. 2007. Microglia-mediated neurotoxicity: uncovering the molecular mechanisms. *Nat. Rev. Neurosci.* 8:57–69. https://doi.org/10.1038/nrn2038

Bohlen, C.J., F.C. Bennett, A.F. Tucker, H.Y. Collins, S.B. Mulinyawe, and B.A. Barres. 2017. Diverse Requirements for Microglial Survival, Specification, and Function Revealed by Defined-Medium Cultures. *Neuron.* 94: 759–773.e8. https://doi.org/10.1016/j.neuron.2017.04.043

Brambilla, R., J.J. Ashbaugh, R. Magliozzi, A. Dellarole, S. Karmally, D.E. Szymkowski, and J.R. Bethea. 2011. Inhibition of soluble tumour necrosis factor is therapeutic in experimental autoimmune encephalomyelitis and promotes axon preservation and remyelination. *Brain.* 134: 2736–2754. https://doi.org/10.1093/brain/awr199

Cantuti-Castelvetri, L., D. Fitzner, M. Bosch-Queralt, M.T. Weil, M. Su, P. Sen, T. Ruhwedel, M. Mitkovski, G. Trendelenburg, D. Lütjohann, et al. 2018.

Defective cholesterol clearance limits remyelination in the aged central nervous system. *Science.* 359:684–688. https://doi.org/10.1126/science.aan4183

Cardona, A., S. Saalfeld, J. Schindelin, I. Arganda-Carreras, S. Preibisch, M. Longair, P. Tomancak, V. Hartenstein, and R.J. Douglas. 2012. TrakEM2 software for neural circuit reconstruction. *PLoS One.* 7:e38011. https://doi.org/10.1371/journal.pone.0038011

Carpenter, A.E., T.R. Jones, M.R. Lamprecht, C. Clarke, I.H. Kang, O. Friman, D.A. Guertin, J.H. Chang, R.A. Lindquist, J. Moffat, et al. 2006. CellProfiler: image analysis software for identifying and quantifying cell phenotypes. *Genome Biol.* 7:R100. https://doi.org/10.1186/gb-2006-7-10-r100

Cox, J., M.Y. Hein, C.A. Luber, I. Paron, N. Nagaraj, and M. Mann. 2014. Accurate proteome-wide label-free quantification by delayed normalization and maximal peptide ratio extraction, termed MaxLFQ. *Mol. Cell. Proteomics.* 13:2513–2526. https://doi.org/10.1074/mcp.M113.031591

Czopka, T., and D.A. Lyons. 2011. Dissecting mechanisms of myelinated axon formation using zebrafish. *Methods Cell Biol.* 105:25–62. https://doi.org/10.1016/B978-0-12-381320-6.00002-3

Dendrou, C.A., L. Fugger, and M.A. Friese. 2015. Immunopathology of multiple sclerosis. *Nat. Rev. Immunol.* 15:545–558. https://doi.org/10.1038/nri3871

Dombrowski, Y., T. O'Hagan, M. Dittmer, R. Penalva, S.R. Mayoral, P. Bankhead, S. Fleville, G. Eleftheriadis, C. Zhao, M. Naughton, et al. 2017. Regulatory T cells promote myelin regeneration in the central nervous system. *Nat. Neurosci.* 20:674–680. https://doi.org/10.1038/nn.4528

Ellett, F., L. Pase, J.W. Hayman, A. Andrianopoulos, and G.J. Lieschke. 2011. mpeg1 promoter transgenes direct macrophage-lineage expression in zebrafish. *Blood.* 117:e49–e56. https://doi.org/10.1182/blood-2010-10-314120

Fard, M.K., F. van der Meer, P. Sánchez, L. Cantuti-Castelvetri, S. Mandad, S. Jäkel, E.F. Fornasiero, S. Schmitt, M. Ehrlich, L. Starost, et al. 2017. BCAS1 expression defines a population of early myelinating oligodendrocytes in multiple sclerosis lesions. *Sci. Transl. Med.* 9:eaam7816. https://doi.org/10.1126/scitranslmed.aam7816

Foote, A.K., and W.F. Blakemore. 2005. Inflammation stimulates remyelination in areas of chronic demyelination. *Brain.* 128:528–539. https://doi.org/10.1093/brain/awh417

Franklin, R.J.M., and C. Ffrench-Constant. 2017. Regenerating CNS myelin - from mechanisms to experimental medicines. *Nat. Rev. Neurosci.* 18:753–769. https://doi.org/10.1038/nrn.2017.136

Han, M.H., S.I. Hwang, D.B. Roy, D.H. Lundgren, J.V. Price, S.S. Ousman, G.H. Fernald, B. Gerlitz, W.H. Robinson, S.E. Baranzini, et al. 2008. Proteomic analysis of active multiple sclerosis lesions reveals therapeutic targets. *Nature.* 451:1076–1081. https://doi.org/10.1038/nature06559

Hill, R.A., J. Medved, K.D. Patel, and A. Nishiyama. 2014. Organotypic slice cultures to study oligodendrocyte dynamics and myelination. *J. Vis. Exp.* 25:e51835.

Hochreiter-Hufford, A., and K.S. Ravichandran. 2013. Clearing the dead: apoptotic cell sensing, recognition, engulfment, and digestion. *Cold Spring Harb. Perspect. Biol.* 5:a008748. https://doi.org/10.1101/cshperspect.a008748

Hua, Y., P. Laserstein, and M. Helmstaedter. 2015. Large-volume en-bloc staining for electron microscopy-based connectomics. *Nat. Commun.* 6:7923. https://doi.org/10.1038/ncomms8923

Jäkel, S., E. Agirre, A. Mendanha Falcão, D. van Bruggen, K.W. Lee, I. Knuesel, D. Malhotra, C. Ffrench-Constant, A. Williams, and G. Castelo-Branco. 2019. Altered human oligodendrocyte heterogeneity in multiple sclerosis. *Nature.* 566:543–547. https://doi.org/10.1038/s41586-019-0903-2

Jeffery, N.D., and W.F. Blakemore. 1995. Remyelination of mouse spinal cord axons demyelinated by local injection of lysolecithin. *J. Neurocytol.* 24:775–781. https://doi.org/10.1007/BF01191213

Kanther, M., X. Sun, M. Mühlbauer, L.C. Mackey, E.J. Flynn III, M. Bagnat, C. Jobin, and J.F. Rawls. 2011. Microbial colonization induces dynamic temporal and spatial patterns of NF-κB activation in the zebrafish digestive tract. *Gastroenterology.* 141:197–207. https://doi.org/10.1053/j.gastro.2011.03.042

Karamita, M., C. Barnum, W. Möbius, M.G. Tansey, D.E. Szymkowski, H. Lassmann, and L. Probert. 2017. Therapeutic inhibition of soluble brain TNF promotes remyelination by increasing myelin phagocytosis by microglia. *JCI Insight.* 2:87455. https://doi.org/10.1172/jci.insight.87455

Karttunen, M.J., T. Czopka, M. Goedhart, J.J. Early, and D.A. Lyons. 2017. Regeneration of myelin sheaths of normal length and thickness in the zebrafish CNS correlates with growth of axons in caliber. *PLoS One.* 12:e0178058. https://doi.org/10.1371/journal.pone.0178058

Kawai, T., and S. Akira. 2007. Signaling to NF-kappaB by Toll-like receptors. *Trends Mol. Med.* 13:460–469. https://doi.org/10.1016/j.molmed.2007.09.002

Keough, M.B., S.K. Jensen, and V.W. Yong. 2015. Experimental demyelination and remyelination of murine spinal cord by focal injection of lysolecithin. *J. Vis. Exp.* (97). https://doi.org/10.3791/52679

Kirby, B.B., N. Takada, A.J. Latimer, J. Shin, T.J. Carney, R.N. Kelsh, and B. Appel. 2006. In vivo time-lapse imaging shows dynamic oligodendrocyte progenitor behavior during zebrafish development. *Nat. Neurosci.* 9:1506–1511. https://doi.org/10.1038/nn1803

Kotter, M.R., W.W. Li, C. Zhao, and R.J. Franklin. 2006. Myelin impairs CNS remyelination by inhibiting oligodendrocyte precursor cell differentiation. *J. Neurosci.* 26:328–332. https://doi.org/10.1523/JNEUROSCI.2615-05.2006

Kubota, Y., J. Sohn, S. Hatada, M. Schurr, J. Straehle, A. Gour, R. Neujahr, T. Miki, S. Mikula, and Y. Kawaguchi. 2018. A carbon nanotube tape for serial-section electron microscopy of brain ultrastructure. *Nat. Commun.* 9:437. https://doi.org/10.1038/s41467-017-02768-7

Lloyd, A.F., and V.E. Miron. 2019. The pro-remyelination properties of microglia in the central nervous system. *Nat. Rev. Neurol.* 15:447–458. https://doi.org/10.1038/s41582-019-0184-2

Lloyd, A.F., C.L. Davies, R.K. Holloway, Y. Labrak, G. Ireland, D. Carradori, A. Dillenburg, E. Borger, D. Soong, J.C. Richardson, et al. 2019. Central nervous system regeneration is driven by microglia necroptosis and repopulation. *Nat. Neurosci.* 22:1046–1052. https://doi.org/10.1038/s41593-019-0418-z

Mensch, S., M. Baraban, R. Almeida, T. Czopka, J. Ausborn, A. El Manira, and D.A. Lyons. 2015. Synaptic vesicle release regulates myelin sheath number of individual oligodendrocytes in vivo. *Nat. Neurosci.* 18:628–630. https://doi.org/10.1038/nn.3991

Miron, V.E., A. Boyd, J.-W. Zhao, T.J. Yuen, J.M. Ruckh, J.L. Shadrach, P. van Wijngaarden, A.J. Wagers, A. Williams, R.J.M. Franklin, and C. Ffrench-Constant. 2013. M2 microglia and macrophages drive oligodendrocyte differentiation during CNS remyelination. *Nat. Neurosci.* 16:1211–1218. https://doi.org/10.1038/nn.3469

Münzel, E.J., C.G. Becker, T. Becker, and A. Williams. 2014. Zebrafish regenerate full thickness optic nerve myelin after demyelination, but this fails with increasing age. *Acta Neuropathol. Commun.* 2:77. https://doi.org/10.1186/s40478-014-0077-y

Nguyen-Chi, M., Q.T. Phan, C. Gonzalez, J.F. Dubremetz, J.P. Levraud, and G. Lutfalla. 2014. Transient infection of the zebrafish notochord with E. coli induces chronic inflammation. *Dis. Model. Mech.* 7:871–882. https://doi.org/10.1242/dmm.014498

Ogryzko, N.V., E.E. Hoggett, S. Solaymani-Kohal, S. Tazzyman, T.J. Chico, S.A. Renshaw, and H.L. Wilson. 2014. Zebrafish tissue injury causes upregulation of interleukin-1 and caspase-dependent amplification of the inflammatory response. *Dis. Model. Mech.* 7:259–264. https://doi.org/10.1242/dmm.013029

Oosterhof, N., L.E. Kuil, H.C. van der Linde, S.M. Burm, W. Berdowski, W.F.J. van Ijcken, J.C. van Swieten, E.M. Hol, M.H.G. Verheijen, and T.J. van Ham. 2018. Colony-Stimulating Factor 1 Receptor (CSF1R) Regulates Microglia Density and Distribution, but Not Microglia Differentiation In Vivo. *Cell Reports.* 24:1203–1217.e6. https://doi.org/10.1016/j.celrep.2018.06.113

Perez-Riverol, Y., A. Csordas, J. Bai, M. Bernal-Llinares, S. Hewapathirana, D.J. Kundu, A. Inuganti, J. Griss, G. Mayer, M. Eisenacher, et al. 2019. The PRIDE database and related tools and resources in 2019: improving support for quantification data. *Nucleic Acids Res.* https://doi.org/10.1093/nar/gky1106

Perry, V.H., and J. Teeling. 2013. Microglia and macrophages of the central nervous system: the contribution of microglia priming and systemic inflammation to chronic neurodegeneration. *Semin. Immunopathol.* 35:601–612. https://doi.org/10.1007/s00281-013-0382-8

Plemel, J.R., W.Q. Liu, and V.W. Yong. 2017. Remyelination therapies: a new direction and challenge in multiple sclerosis. *Nat. Rev. Drug Discov.* 16:617–634. https://doi.org/10.1038/nrd.2017.115

Rappsilber, J., Y. Ishihama, and M. Mann. 2003. Stop and go extraction tips for matrix-assisted laser desorption/ionization, nanoelectrospray, and LC/MS sample pretreatment in proteomics. *Anal. Chem.* 75:663–670. https://doi.org/10.1021/ac026117i

Reich, D.S., C.F. Lucchinetti, and P.A. Calabresi. 2018. Multiple Sclerosis. *N. Engl. J. Med.* 378:169–180. https://doi.org/10.1056/NEJMra1401483

Schindelin, J., I. Arganda-Carreras, E. Frise, V. Kaynig, M. Longair, T. Pietzsch, S. Preibisch, C. Rueden, S. Saalfeld, B. Schmid, et al. 2012. Fiji: an open-source platform for biological-image analysis. *Nat. Methods.* 9:676–682. https://doi.org/10.1038/nmeth.2019

Sloane, J.A., C. Batt, Y. Ma, Z.M. Harris, B. Trapp, and T. Vartanian. 2010. Hyaluronan blocks oligodendrocyte progenitor maturation and remyelination through TLR2. *Proc. Natl. Acad. Sci. USA.* 107:11555–11560. https://doi.org/10.1073/pnas.1006496107

Steeland, S., S. Van Ryckeghem, G. Van Imschoot, R. De Rycke, W. Toussaint, L. Vanhoutte, C. Vanhove, F. De Vos, R.E. Vandenbroucke, and C. Libert. 2017. TNFR1 inhibition with a Nanobody protects against EAE development in mice. *Sci. Rep.* 7:13646. https://doi.org/10.1038/s41598-017-13984-y

Syed, Y.A., E. Hand, W. Möbius, C. Zhao, M. Hofer, K.A. Nave, and M.R. Kotter. 2011. Inhibition of CNS remyelination by the presence of semaphorin 3A. *J. Neurosci.* 31:3719–3728. https://doi.org/10.1523/JNEUROSCI.4930-10.2011

Takeda, K., T. Kaisho, and S. Akira. 2003. Toll-like receptors. *Annu. Rev. Immunol.* 21:335–376. https://doi.org/10.1146/annurev.immunol.21.120601.141126

Thetiot, M., R. Ronzano, M.S. Aigrot, C. Lubetzki, and A. Desmazières. 2019. Preparation and Immunostaining of Myelinating Organotypic Cerebellar Slice Cultures. *J. Vis. Exp.* (145). https://doi.org/10.3791/59163

Tsarouchas, T.M., D. Wehner, L. Cavone, T. Munir, M. Keatinge, M. Lambertus, A. Underhill, T. Barrett, E. Kassapis, N. Ogryzko, et al. 2018. Dynamic control of proinflammatory cytokines Il-1β and Tnf-α by macrophages in zebrafish spinal cord regeneration. *Nat. Commun.* 9:4670. https://doi.org/10.1038/s41467-018-07036-w

Tusher, V.G., R. Tibshirani, and G. Chu. 2001. Significance analysis of microarrays applied to the ionizing radiation response. *Proc. Natl. Acad. Sci. USA.* 98:5116–5121. https://doi.org/10.1073/pnas.091062498

Tyanova, S., T. Temu, P. Sinitcyn, A. Carlson, M.Y. Hein, T. Geiger, M. Mann, and J. Cox. 2016. The Perseus computational platform for comprehensive analysis of (prote)omics data. *Nat. Methods.* 13:731–740. https://doi.org/10.1038/nmeth.3901

van der Vaart, M., J.J. van Soest, H.P. Spaink, and A.H. Meijer. 2013. Functional analysis of a zebrafish myd88 mutant identifies key transcriptional components of the innate immune system. *Dis. Model. Mech.* 6:841–854. https://doi.org/10.1242/dmm.010843

van Oosten, B.W., F. Barkhof, L. Truyen, J.B. Boringa, F.W. Bertelsmann, B.M. von Blomberg, J.N. Woody, H.P. Hartung, and C.H. Polman. 1996. Increased MRI activity and immune activation in two multiple sclerosis patients treated with the monoclonal anti-tumor necrosis factor antibody cA2. *Neurology.* 47:1531–1534. https://doi.org/10.1212/WNL.47.6.1531

Wang, C., and M.R. Kotter. 2018. Experimental Demyelination and Remyelination of Murine Spinal Cord by Focal Injection of Lysolecithin. *Methods Mol. Biol.* 1791:233–241. https://doi.org/10.1007/978-1-4939-7862-5_18

Wesche, H., W.J. Henzel, W. Shillinglaw, S. Li, and Z. Cao. 1997. MyD88: an adapter that recruits IRAK to the IL-1 receptor complex. *Immunity.* 7:837–847. https://doi.org/10.1016/S1074-7613(00)80402-1

Wiśniewski, J.R., A. Zougman, N. Nagaraj, and M. Mann. 2009. Universal sample preparation method for proteome analysis. *Nat. Methods.* 6:359–362. https://doi.org/10.1038/nmeth.1322

Yeung, M.S.Y., M. Djelloul, E. Steiner, S. Bernard, M. Salehpour, G. Possnert, L. Brundin, and J. Frisén. 2019. Dynamics of oligodendrocyte generation in multiple sclerosis. *Nature.* 566:538–542. https://doi.org/10.1038/s41586-018-0842-3

Zhang, H., A.A. Jarjour, A. Boyd, and A. Williams. 2011. Central nervous system remyelination in culture--a tool for multiple sclerosis research. *Exp. Neurol.* 230:138–148. https://doi.org/10.1016/j.expneurol.2011.04.009

# Supplemental material

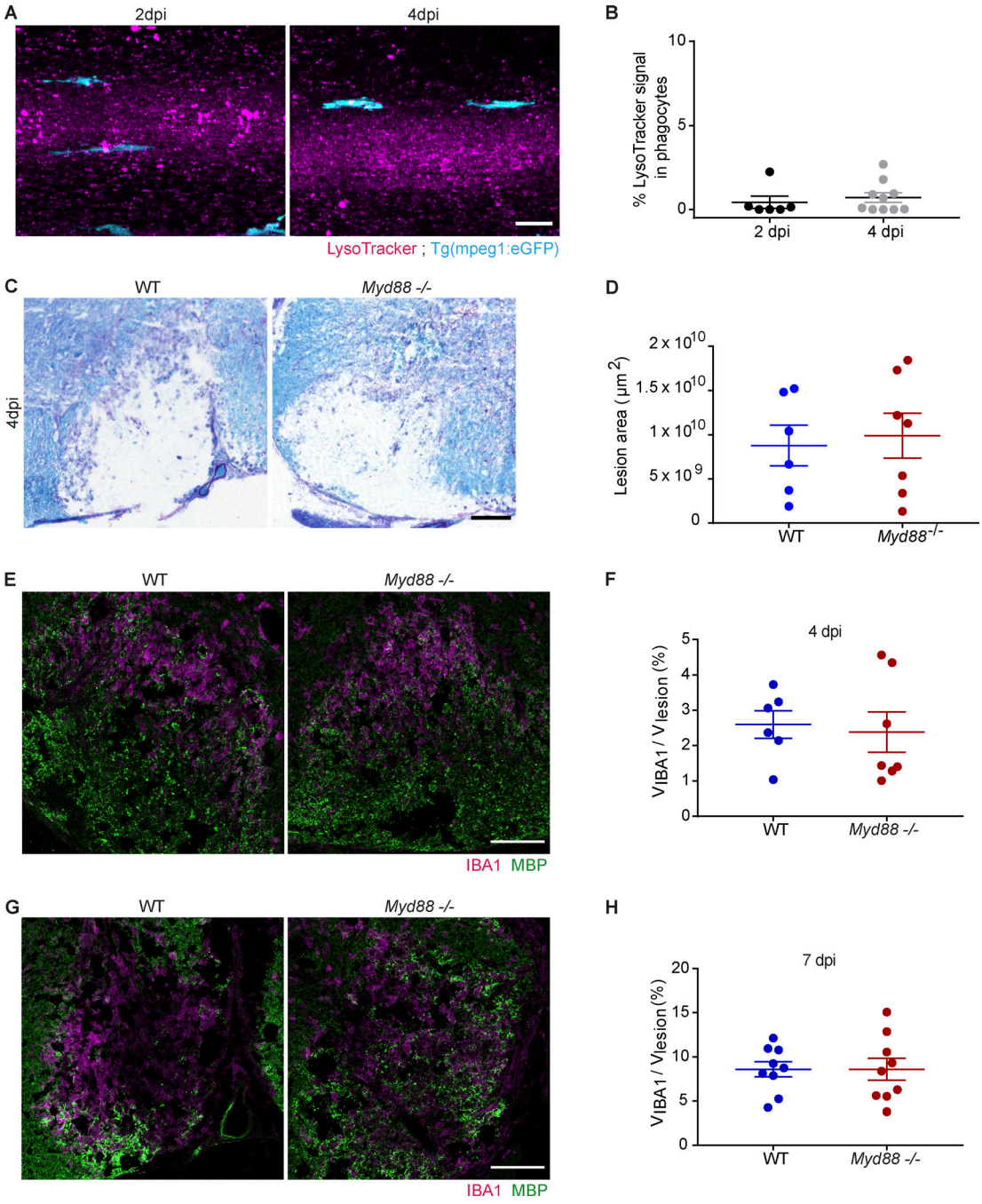


Figure S1. **Characterization of WT and *Myd88*$^{-/-}$ zebrafish and mice in noninjected and injected conditions. (A)** Confocal maximum intensity z-projections of the spinal cord at 2 and 4 dpi showing lysosomes (magenta) in the phagocytes (cyan) in noninjected WT larvae. **(B)** Quantification of the amount of lysosomes in phagocytes determined by the colocalized signal of LysoTracker with mpeg1:eGFP relative to the total amount of mpeg1:eGFP signal. *n* = 6 or 10 animals. **(C and D)** Luxol Fast Blue staining of mouse spinal cord lesions at 4 dpi. Lesion area was determined by the lack of staining. *n* = 6 or 7 lesions. **(E and F)** IBA1$^{+}$ microglia/macrophages were recruited to LPC-induced demyelinated lesions of both WT and *Myd88*$^{-/-}$ mice at 4 dpi. *n* = 6 or 7 lesions. **(G and H)** At 7 dpi, the proportion of the volume (V) occupied by IBA1$^{+}$ cells in the lesions was similar in *Myd88*$^{-/-}$ and WT mice. *n* = 9 lesions. All data are mean ± SEM (error bars). Scale bars: 20 µm in A; 50 µm in C; 100 µm in E and G.

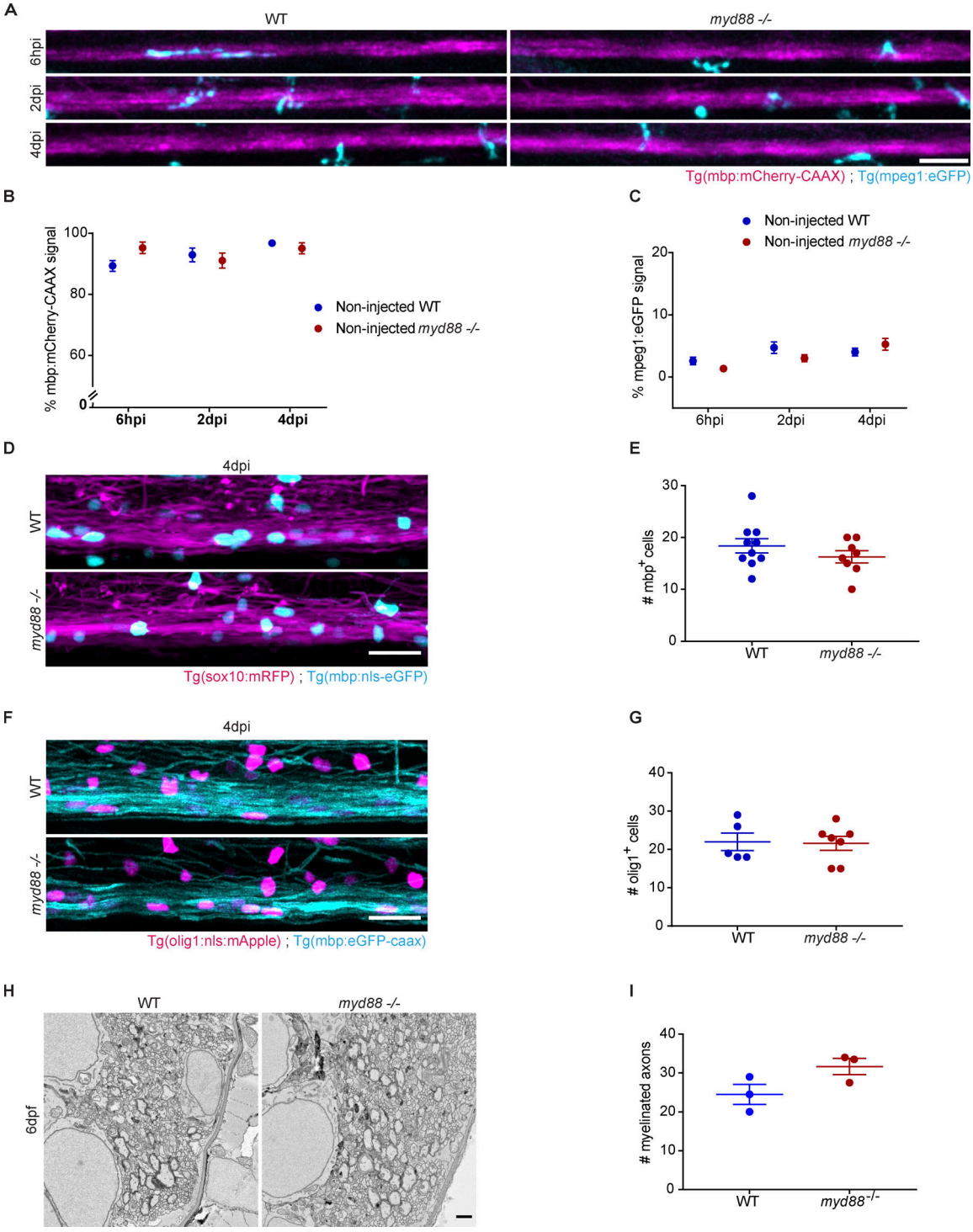


Figure S2. **Myelination and phagocyte infiltration are not affected in *myd88*$^{-/-}$ noninjected larvae. (A)** Confocal maximum intensity z-projections of the spinal cord of noninjected larvae over time, showing the myelinated spinal cord (magenta) and phagocytes (cyan) in WT and *myd88*$^{-/-}$ larvae. **(B)** Quantification of myelination determined by the total amount of mbp:mCherry-CAAX signal in the dorsal spinal cord. *n* = 15–19, 11–17, and 13–17at 6 hpi, 2 dpi, and 4 dpi, respectively. **(C)** Quantification of phagocyte infiltration in the spinal cord determined by the total amount of mpeg1:eGFP signal. *n* = 15–19, 11–17, and 13–17at 6 hpi, 2 dpi, and 4 dpi, respectively. **(D)** Confocal maximum intensity z-projections of the spinal cord of noninjected larvae at 4 dpi, showing the myelinated spinal cord (magenta) and the nuclei of mature oligodendrocytes (cyan) in WT and *myd88*$^{-/-}$ larvae. **(E)** Quantification of the number of mature oligodendrocytes present in the spinal cord determined by the number of mbp:nls-eGFP–positive nuclei. *n* = 10 or 8 animals. **(F)** Confocal maximum intensity z-projections of the spinal cord of noninjected larvae at 4 dpi, showing the myelinated spinal cord (cyan) and the nuclei of oligodendrocyte precursor cells (magenta) in WT and *myd88*$^{-/-}$ larvae. **(G)** Quantification of the number of OPCs present in the spinal cord determined by the number of olig1:nls-mApple–positive nuclei. *n* = 5 or 7 animals. **(H and I)** Electron micrographs of 6 dpf noninjected dorsal spinal cord cross sections in WT and *myd88*$^{-/-}$ larvae. Total number of myelinated axons was determined in a representative cross section per animal. *n* = 3 animals. All data are mean ± SEM (error bars). Scale bars: 50 µm in A; 20 µm in D and F; 1 µm in H.

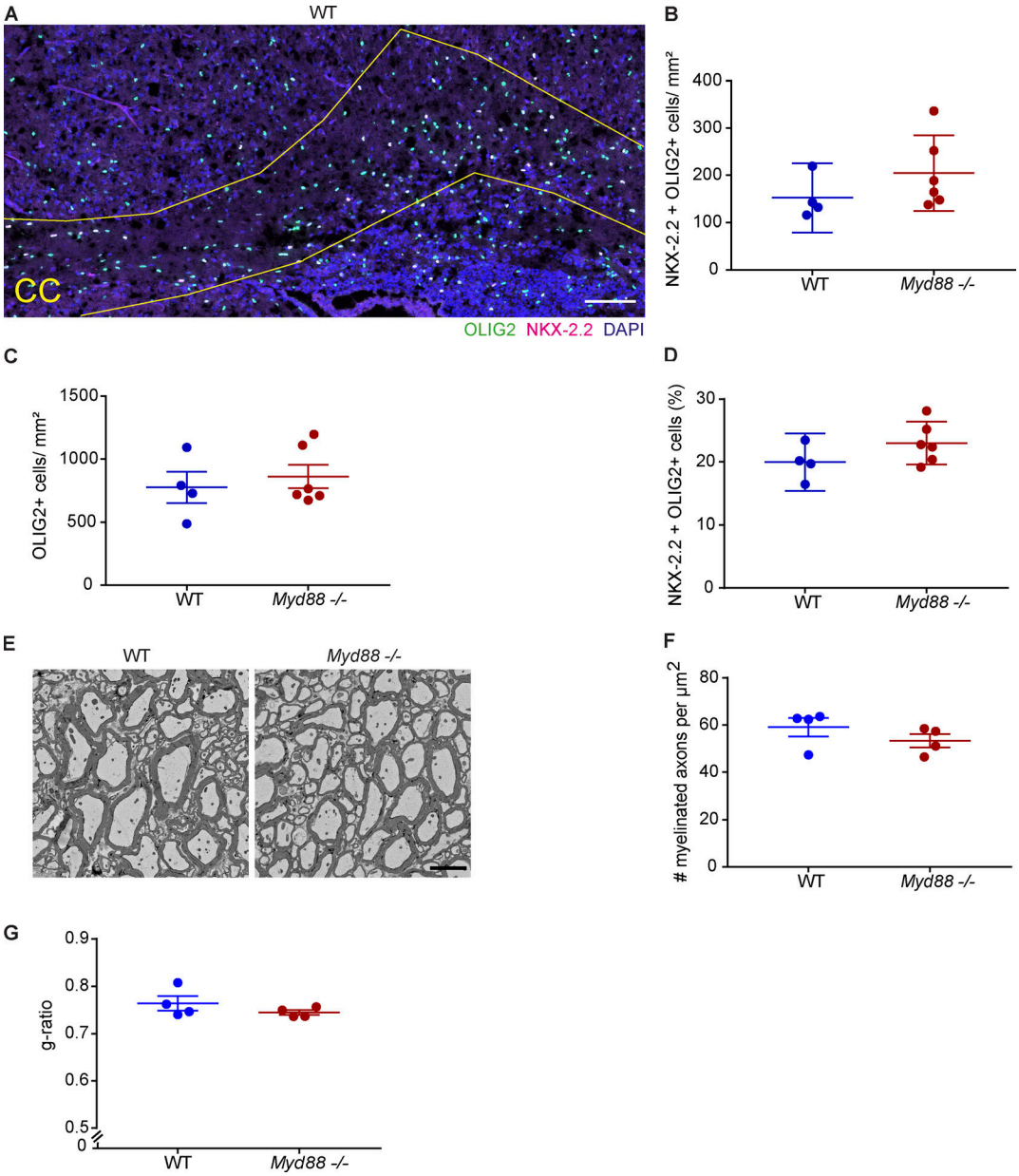


Figure S3. **Oligodendrogenesis is not affected in MyD88-deficient mice. (A)** The numbers of oligodendrocytes and OPCs in the corpus callosum (CC) of P7 *Myd88*$^{-/-}$ and WT mice were similar. The nuclei of OPCs were identified by the expression of both transcription factors NKX-2.2 and OLIG2. **(B)** The cell density of OPCs in the CC was similar. **(C)** The cell density of oligodendrocyte-lineage cells in the CC was similar. **(D)** The proportion of OPCs among oligodendrocyte-lineage cells was similar, suggesting normal OPC proliferation in the developing brain of MyD88-deficient mice. *n* = 4 or 6 animals. **(E–G)** Electron micrographs of mouse spinal cord cross sections of 7–8-wk-old WT and *Myd88*$^{-/-}$ mice. The number of myelinated axons was determined in two or three 1,600-µm$^2$ areas per animal. Myelin thickness was determined by g-ratio analysis in 225 µm$^2$ per animal. *n* = 4 animals. Data are mean ± 95% CI (error bars) in B, C, and D or SEM in F and G. Scale bar: 100 µm in A; 2 µm in E.

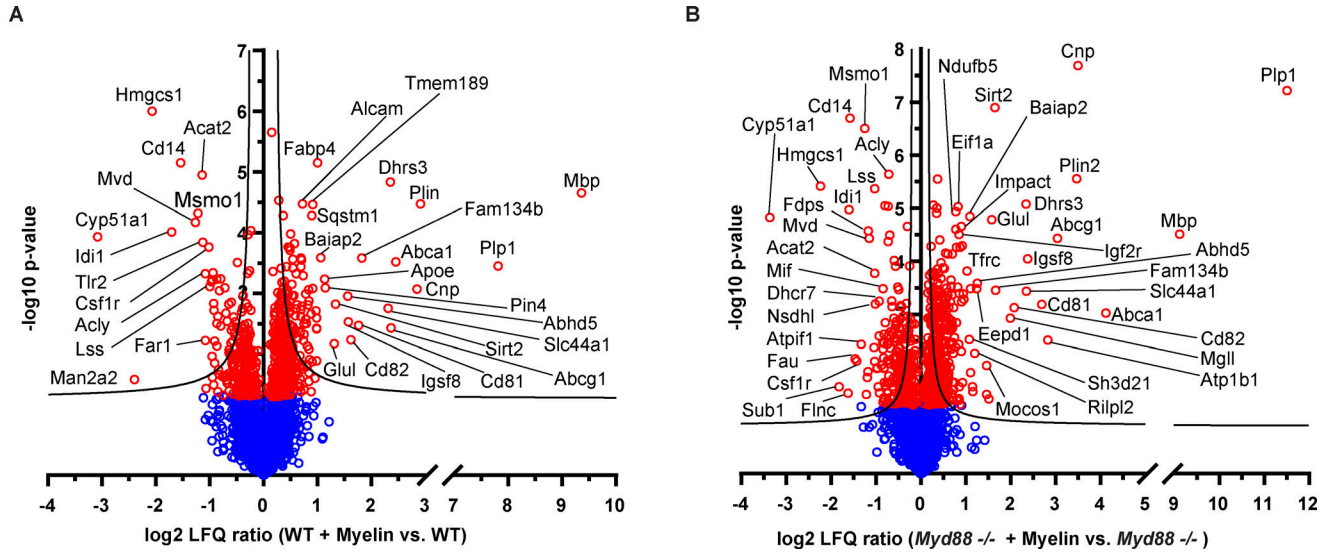


Figure S4. **Proteome analysis of cultured microglia. (A and B)** Volcano plots of regulated proteins in myelin-treated versus vehicle-treated WT microglia and myelin-treated versus vehicle-treated *Myd88*$^{-/-}$ microglia, respectively. The negative $\log_{10}$ transformed P value is plotted against the $\log_2$ transformed LFQ intensity ratios for each protein. Proteins with a P value <0.05 are indicated as red circles, whereas proteins with a P value >0.05 are indicated as blue circles. The hyperbolic curves indicate the threshold of a permutation-based FDR correction for multiple hypotheses (FDR: P = 0.05, s0 = 0.1).

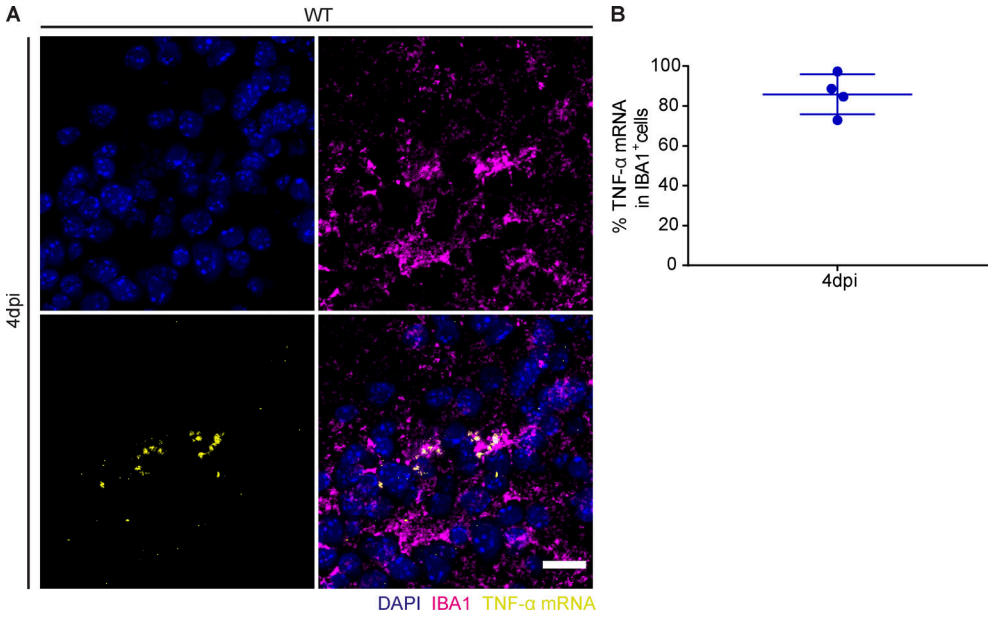


Figure S5. **Quantification of TNF-α in IBA1⁺ cells. (A and B)** Confocal maximum intensity z-projections of combined RNAscope in situ hybridization and IHC to visualize TNF-α transcript and IBA1 protein, respectively, in WT mouse spinal cord lesions at 4 dpi. The amount of TNF-α in IBA1⁺ cells was determined by the colocalized signal of TNF-α with IBA1 per total amount of TNF-α signal. *n* = 4 lesions. All data are mean ± SEM (error bars). Scale bar: 20 µm.

Video 1. **Phagocytes in a demyelinating lesion in WT zebrafish larvae at 2 dpi.** Time-lapse imaging of WT double transgenic Tg(*mbp:mCherry-CAAX*) and Tg(*mpeg1:eGFP*) larvae showing a phagocyte actively taking up and stripping off myelin from the axonal tracts in an LPC-induced lesion at 2 dpi. Time-lapse imaging was performed for 2 h, with a 12-min interval between frames. Scale bar: 20 µm.

Video 2. **Phagocytes in a demyelinating lesion in WT zebrafish larvae at 3 dpi.** Time-lapse imaging of WT double transgenic Tg(*mbp:mCherry-CAAX*) and Tg(*mpeg1:eGFP*) larvae showing highly motile phagocytes handling myelin debris in an LPC-induced lesion at 3 dpi. Time-lapse imaging was performed for 2 h, with a 10-min interval between frames. Scale bar: 20 µm.

Video 3. **Phagocytes in a demyelinating lesion in *myd88*$^{-/-}$ zebrafish larvae at 3 dpi.** Time-lapse imaging of *myd88*$^{-/-}$ double transgenic Tg(*mbp:mCherry-CAAX*) and Tg(*mpeg1:eGFP*) larvae showing the presence of amoeboid stationary phagocytes in an LPC-induced lesion at 3 dpi. Time-lapse imaging was performed for 2 h, with a 10-min interval between frames. Scale bar: 20 µm.

**Tables S1–S3 are provided online as separate files. Table S1 lists up-regulated proteins induced by myelin debris in cultured WT and Myd88$^{-/-}$ microglia. Table S2 lists the number of total regulated proteins from proteomics. Table S3 lists up-regulated proteins induced by myelin debris in cultured WT microglia.**